



1           **Modelling the firn thickness evolution during the last deglaciation:**  
2                           **constrains on sensitivity to temperature and impurities**

3

4 Camille Bréant <sup>1,2</sup>, Patricia Martinerie <sup>2</sup>, Anaïs Orsi <sup>1</sup>, Laurent Arnaud <sup>2</sup> and Amaëlle Landais <sup>1</sup>

5

6 <sup>1</sup>Laboratoire des Sciences du Climat et de l'Environnement, UMR8212, CEA-CNRS-UPS/IPSL, Gif-sur-Yvette,  
7 France

8 <sup>2</sup>Univ. Grenoble Alpes/CNRS, Laboratoire de Glaciologie et de Géophysique de l'Environnement (LGGE), UMR  
9 5183, Grenoble, F-38041, France

10

11 The transformation of snow into ice is a complex phenomenon difficult to model. Depending on  
12 surface temperature and accumulation rate, it may take several decades to millennia for air to be  
13 entrapped in ice. The air is thus always younger than the surrounding ice. The resulting gas-ice age  
14 difference is essential to document the phasing between CO<sub>2</sub> and temperature changes especially  
15 during deglaciations. The air trapping depth can be inferred in the past using a firn densification  
16 model, or using  $\delta^{15}\text{N}$  of air measured in ice cores.

17 All firn densification models applied to deglaciations show a large disagreement with  $\delta^{15}\text{N}$   
18 measurements in several sites of East Antarctica, predicting larger firn thickness during the Last  
19 Glacial Maximum, whereas  $\delta^{15}\text{N}$  suggests a reduced firn thickness compared to the Holocene. We  
20 present here modifications of the LGGE firn densification model, which significantly reduce the  
21 model-data mismatch for the gas trapping depth evolution over the last deglaciation, while  
22 preserving the good agreement between measured and modelled modern firn density profiles. In  
23 particular, we introduce a dependency of the activation energy to temperature and impurities in  
24 the firn densification rate calculation. The temperature influence reflects the existence of different  
25 mechanisms for firn compaction at different temperatures. We show that both the new  
26 temperature parameterization and the influence of impurities contribute to the increased  
27 agreement between modelled and measured  $\delta^{15}\text{N}$  evolution during the last deglaciation at sites  
28 with low temperature and low accumulation rate, such as Dome C or Vostok. However, the inclusion  
29 of impurities effects deteriorates the agreement between modelled and measured  $\delta^{15}\text{N}$  evolution  
30 in Greenland and Antarctic sites with high accumulation.

31

32           1. Introduction

33

34 Ice cores are important tools to decipher the influence of different forcings on climate evolution.



35 They are particularly useful to depict the past variations of polar temperature and greenhouse  
36 gases. The longest record covers 8 last glacial – interglacial cycles (EPICA community members,  
37 2004; Jouzel et al., 2007; Loulergue et al., 2008; Lüthi et al., 2008) and very high resolution climate  
38 records can be retrieved from ice cores drilled in high accumulation regions (Marcott et al., 2014;  
39 Rhodes et al., 2015; WAIS Divide Project Members, 2013, 2015).

40

41 Polar ice is a porous medium, and contains bubbles filled with ancient atmospheric air, allowing the  
42 reconstruction of the atmospheric composition in the past. The air is trapped at about 100 m under  
43 the ice sheet surface. Above that depth, the interstitial air in firn pores remains in contact with the  
44 atmosphere. Consequently, the air is always younger than the surrounding ice and this age  
45 difference,  $\Delta_{age}$ , can reach several millennia at the low temperature and accumulation rate sites of  
46 East Antarctica.

47

48 A precise determination of  $\Delta_{age}$  is essential to quantify the link between temperature changes  
49 recorded in the water isotopic measurements on the ice phase and greenhouse gas concentrations  
50 recorded in the gas phase. Still, quantifying the temporal relationship between changes in  
51 greenhouse gas concentrations in air bubbles and changes in polar temperature recorded in the  
52 isotopic composition of the ice is not straightforward. One way to address this question goes  
53 through the development of firn densification models that depict the progressive densification of  
54 snow to ice, and the associated decrease of porosity. Below a certain threshold density, the pores  
55 seal off and the air is trapped. The firn densification models thus calculate the Lock-in Depth  
56 (hereafter LID) according to surface climatic conditions. A higher temperature accelerates the firn  
57 metamorphism and leads to a lower LID. On the other hand, a higher snow accumulation at the  
58 surface will have the effect of increasing the firn sinking speed and hence the LID. In practice,  
59 accumulation usually increases when temperature increases, and both effects partially compensate  
60 each other, with the temperature effect being dominant in the current densification models for the  
61 LID simulation over glacial – interglacial transitions in deep drilling sites of the East Antarctic plateau.  
62 A first class of densification models is based on an empirical approach to link accumulation rate and  
63 temperature at different polar sites to densification rates (allowing the match between the  
64 modelled and the measured density profiles) (e.g. Herron and Langway, 1980). The Herron and  
65 Langway (1980) model assumes that the porosity (air space in the firn) directly relates to the stress  
66 induced by the overlying snow, hence the accumulation rate. A temperature dependence following  
67 an Arrhenius law is also implemented to account for a more rapid compaction at higher



68 temperature. Finally, the exact model sensitivity to temperature and accumulation rate is adjusted  
69 empirically in order to simulate observed density profiles. Measured density profiles exhibit  
70 different densification rates above and below 550 kg/m<sup>3</sup> so that different empirical laws are used  
71 for densities above and below this threshold. Indeed, 550 kg/m<sup>3</sup> corresponds to the observed  
72 maximum packing density of snow (e. g. Anderson and Benson, 1963), hence to a change in the  
73 driving mechanism of firnification.

74

75 Despite its simple empirical description, and although more sophisticated empirical models have  
76 been developed (Arthern et al., 2010; Helsen et al., 2008; e.g. Li and Zwally, 2004; Ligtenberg et al.,  
77 2015), the Herron and Langway (1980) firn model often provides good quality results and is still used  
78 in a number of ice core studies (e.g. Buizert et al., 2015; Overly et al., 2015). However, its validity is  
79 questionable when used outside of its range of calibration, such as glacial periods at cold sites of  
80 the East Antarctic plateau for which no present-day analogue exists. As a consequence firn models  
81 including a more physical description of densification have been developed (e.g. Arnaud et al., 2000;  
82 Salamatin et al., 2009). The model developed over the past 30 years at LGGE (Arnaud et al., 2000;  
83 Barnola et al., 1991; Goujon et al., 2003; Pimienta, 1987) aims at using a physical approach which  
84 remains sufficiently simple to be used on very long time scales (covering the ice core record length).  
85 More complex models, explicitly representing the material micro-structure have been developed  
86 but require a lot more computing time (Hagenmuller et al., 2015; Miller et al., 2003).

87

88 In parallel to firn densification modelling, past firn LID can also be determined using the  $\delta^{15}\text{N}$   
89 measurements in the air trapped in ice cores. Indeed, in the absence of any abrupt temperature  
90 change at the ice-sheet surface, the  $\delta^{15}\text{N}$  trapped at the bottom of the firn is directly related to the  
91 diffusive column height (DCH). This is due to gravitational settling in the firn following the steady  
92 state barometric equation (Craig et al., 1988; Schwander, 1989; Sowers et al., 1989):

93

$$94 \quad \delta^{15}N_{grav} = \left[ \exp\left(\frac{\Delta mgz}{RT_{mean}}\right) - 1 \right] 1000 \approx \frac{gz}{RT_{mean}} \Delta m \times 1000 \text{ (‰)} \quad (1)$$

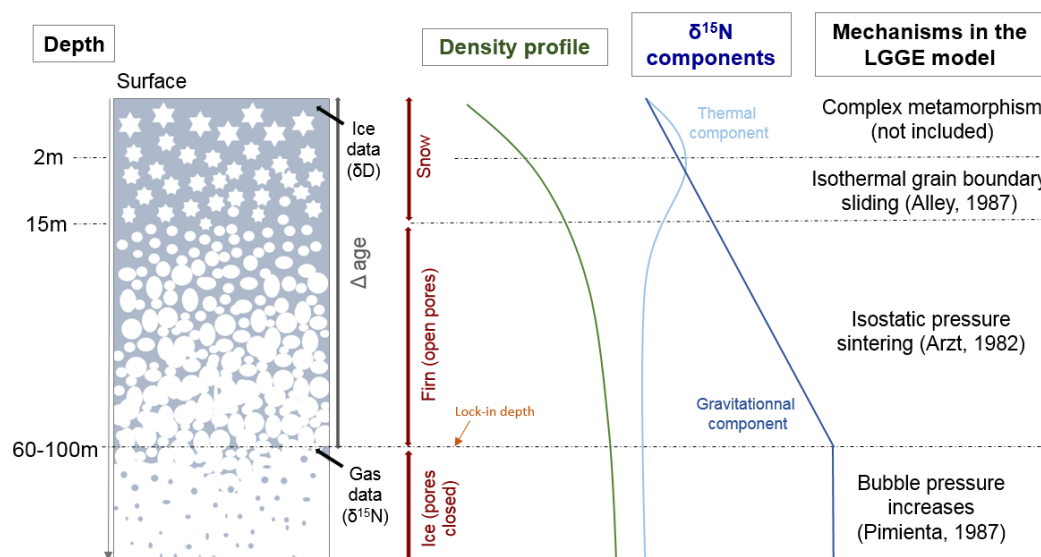
95

96 Where  $\Delta m$  is the mass difference (kg/mol) between <sup>15</sup>N and <sup>14</sup>N,  $g$  is the gravitational acceleration  
97 (9.8 m/s<sup>2</sup>),  $R$  is the gas constant (8.314 J/mol/K),  $T_{mean}$  is the mean firn temperature (K), and  $z$  is the  
98 diffusive column height (m) noted (DCH). In the absence of convection at the top of the firn, the firn  
99 LID is equal to the DCH.

100



101 In Greenland ice cores, where abrupt surface temperature changes occurred during the last glacial  
 102 period and deglaciation,  $\delta^{15}\text{N}$  is also affected by thermal fractionation. An abrupt warming (on the  
 103 order of  $10^\circ\text{C}$  in less than 50 years) indeed induces a transient temperature gradient in the firn of a  
 104 few degrees (Severinghaus et al., 1998; Guillevic et al., 2013; Kindler et al., 2014).  $\delta^{15}\text{N}$  is thus  
 105 modified as  $\delta^{15}\text{N}_{\text{therm}} = \Omega \cdot \Delta T$  and this thermal signal is superimposed on the gravitational one  
 106 ( $\delta^{15}\text{N}_{\text{therm}}$  is at maximum 0.15‰).  
 107



108  
 109  
 110 *Figure 1: Overview of snow densification and influence on the  $\delta^{15}\text{N}$  profile in the absence of any significant convective*  
 111 *zone as observed in most present-day  $\delta^{15}\text{N}$  profiles (Landais et al., 2006; Witrant et al., 2012).*  
 112

113 While models can reproduce the observed  $\delta^{15}\text{N}$  at Greenland sites over the last climatic cycle, a  
 114 strong mismatch is observed for cold Antarctic sites, especially on the East-Antarctic plateau  
 115 (Dreyfus et al., 2010). In particular, both the empirical and physical models predict a decrease of the  
 116 LID during glacial to interglacial transitions (Goujon et al., 2003; Sowers et al., 1992) while the  $\delta^{15}\text{N}$   
 117 evolution indicates an increase of the LID (Capron et al., 2013; Sowers et al., 1992). The decrease in  
 118 the LID in the models is caused by the increase in temperature during the deglaciation, which has a  
 119 stronger impact than the increase in the accumulation rate.  
 120

121 In this study, we test if simple modifications of the LGGE model can reduce the model-data  
 122 mismatch for the LID evolution over the last deglaciation in sites on the East Antarctic plateau. In



123 particular, we explore the underestimation of the firn densification rate at very low temperature  
124 evidenced over the glacial-interglacial transitions (Capron et al., 2013) and the possible influence of  
125 impurity concentration (Freitag et al., 2013; Hörhold et al., 2012). The manuscript is organized as  
126 follows: In the next (second) section we present the physical model with a focus on recent  
127 modifications. In a third section, we confront the model outputs to present-day observed firn  
128 density profiles and  $\delta^{15}\text{N}$  data over the last deglaciation at different polar sites from Greenland and  
129 Antarctica. Section 4 summarizes our conclusions.

130

## 131 2. Densification model description and improvements

132

133 An in-depth description of the LGGE firn densification model is provided in Goujon et al. (2003).  
134 Here we first briefly summarize its content, and then detail the modifications introduced in this  
135 study. The main inputs to the model are temperature and snow accumulation rate. During climatic  
136 transitions occurring at similar or shorter time scales than firnification, the propagation of the  
137 atmospheric temperature signal into the firn has to be taken into account (Schwander et al., 1997).  
138 The thermo-mechanical model comprises four modules. A simple ice sheet flow module calculates  
139 the vertical speed in a 1D firn and ice column. This vertical speed is used in the thermal module to  
140 calculate heat advection. The thermal module solves the heat transfer equation, which combines  
141 heat advection and heat diffusion across the whole ice-sheet thickness. Using the resulting  
142 temperature profile in the firn, the mechanical module evaluates the densification rates resulting  
143 from three successive mechanisms detailed below. Finally, a gas-age module keeps track of snow  
144 layers sinking in a Lagrangian mode and uses a gas trapping criterion in order to evaluate the gas  
145 trapping depth and the ice age – gas age difference ( $\Delta\text{age}$ ).

146 The model does not take into account the complex mechanisms associated with snow  
147 metamorphisms under the influence of strong temperature gradients, wind and sublimation/re-  
148 condensation (Colbeck, 1983; Kojima, 1967; Mellor, 1964). This kind of metamorphism affects the  
149 1-3 meters at the top of the firn and has a minor role on the modelled LID.

150 Below this depth, the densification of snow into ice has been divided in three stages (e.g. Maeno  
151 and Ebinuma, 1983 and references therein; Figure 1). The first stage (from 2 to 15 m depth  
152 approximately), named “snow densification”, corresponds to a rearrangement and packing of snow  
153 grains until approaching the maximum compaction at a density of about  $550 \text{ kg/m}^3$  (or 0.6 on a  
154 unitless scale relative to the density of pure ice) defined as the critical density. The second stage  
155 (from  $\sim 15 \text{ m}$  to  $\sim 60\text{-}100 \text{ m}$  depth) represents the firn densification by sintering associated with visco-



156 plastic deformation. Finally, when the bubbles are closed, the ice densification is driven by the  
 157 difference in pressure between air trapped in bubbles and the solid ice matrix subject to the weight  
 158 of the overlying firn structure. In reality, the first stage densification mechanism (packing by  
 159 boundary sliding) and the second stage mechanism (pressure sintering) likely coexist at  
 160 intermediate densities. Below we further describe the mechanical structure of the model with a  
 161 focus on recent modifications and refer to Arnaud et al. (2000) and Goujon et al. (2003) for more  
 162 details.

163  
 164 The model uses macroscopic (simplified) mechanical laws, which link the densification speed  
 165 ( $dD_{rel}/dt$ , in terms of relative density ( $D_{rel} = \frac{\rho}{\rho_{ice}}$ )) to its main driving force: the overburden  
 166 pressure of overlying snow. It is important to note that in our model, the accumulation rate  
 167 influences firn densification only through the overburden pressure:

$$169 \quad P(h) = g \int_0^h \rho dz \quad (2)$$

170  
 171 where  $g$  is the gravity constant and  $\rho$  is the density in  $\text{kg/m}^3$ . This differs from the Herron and  
 172 Langway (1980) model where the effect of accumulation rate is adjusted and expressed with a  
 173 different power law for snow and firn densification rates. In porous materials, the overburden  
 174 pressure  $P$  is transmitted through contact areas between grains rather than the entire surface of  
 175 the material. This is expressed by replacing  $P$  with an effective pressure  $P_{eff}$  in mechanical stress-  
 176 strain laws. The relationship between  $P$  and  $P_{eff}$  depends on the material geometry (e.g. Equation  
 177 A4 in Goujon et al., 2003). A higher temperature ( $T$ ) facilitates the deformation of materials, and  
 178 this effect is commonly represented by an Arrhenius law:  $e^{\left(\frac{-Q}{RT}\right)}$  where  $R$  is the gas constant and  $Q$   
 179 an activation energy. The value of the activation energy depends on the underlying physical  
 180 mechanism of deformation. We should note that Arrhenius expressions cannot represent  
 181 deformation effects linked to ice melting. The relationships between densification speed and  
 182 overburden pressure thus take the following general form:

$$184 \quad \frac{dD_{rel}}{dt} = A_0 \times e^{\left(\frac{-Q}{RT}\right)} \times (P_{eff})^n \quad (3)$$

185  
 186 where  $A_0$  represents the dependency of the deformation speed on the material geometry change  
 187 and  $n$  is the stress exponent. In the rest of the manuscript, we will refer to  $A = A_0 \times e^{\left(\frac{-Q}{RT}\right)}$  as the



188 creep parameter.

189

190 2.1 Densification of snow

191

192 During the first stage, the dominant snow densification mechanism is assumed to be isothermal  
193 boundary sliding and the model of Alley (1987) is used (Figure 1). The geometrical approximation  
194 used to build the model is to represent snow as equal size spheres with a number of contacts  
195 between neighbours increasing with density. In the LGGE model, the Alley mechanism is  
196 implemented as Equation A1 in Goujon et al. (2003):

197

$$198 \frac{dD_{rel}}{dt} = \gamma \left( \frac{P}{D_{rel}^2} \right) \left( 1 - \frac{5}{3} \times D_{rel} \right) \quad (4)$$

199

200 It directly relates to Equation (5) in Alley (1987):

201

$$202 \frac{dD_{rel}}{dt} = \frac{2}{15} \times \frac{\lambda}{\nu} \times \frac{R}{r^2} \times \left( 1 - \frac{5}{3} * D_{rel} \right) \times \frac{P}{D_{rel}^2} \quad (5)$$

203

204 where  $\lambda$  is the bond thickness,  $\nu$  the bond viscosity,  $R$  the grain radius and  $r$  the bond radius.  $P$  is  
205 expressed as a function of accumulation and gravity (Equation 2).

206 The important simplification in the LGGE model is the replacement of geometry dependent  
207 parameters, not available for past conditions, with a variable  $\gamma$ , adjusted in order to obtain a  
208 continuous densification rate at the boundary between the first and the second stage of  
209 densification.

210 A first modification in this module consists of extending the Alley (1987) scheme to the upper two  
211 meters of the firn rather than using a constant density value. Indeed, since the model is not able to  
212 describe the metamorphism of the first two meters, we impose by continuity a constant  
213 densification rate equals to its value at 2 m depth.

214 The second modification concerns the transition between the snow and firn densification stages at  
215 the relative density of 0.6. In Equation (4), the term  $\left( 1 - \frac{5}{3} \times D_{rel} \right)$  implies that the densification  
216 speed drops to zero at  $D_{rel} = \frac{3}{5}$  (i.e. 0.6 the maximal compaction density). The second stage of  
217 densification (firn densification) is driven by an important overburden pressure on the contact area  
218 hence associated with a high densification speed. The transition between the sharp decrease of the  
219 densification speed for  $D_{rel}$  values close to 0.6 in the snow densification stage and the high



220 densification speed at the beginning of the firn densification (i.e. in the same range of value for  $D_{rel}$ )  
 221 causes some model instabilities especially at sites with high temperature and accumulation rate. In  
 222 order to improve the model stability, we go back to the definition of the term  $\left(1 - \frac{5}{3} \times D_{rel}\right)$  in the  
 223 initial formulation of Alley (1987). This term relies on a correlation between the coordination  
 224 number (N) and relative density:  $D_{rel} = 10 N$ . We slightly modified this relationship and imposes  $D_{rel} =$   
 225  $10 N - 0.5$  which better matches the data on Figure 1 of Alley (1987). This results in replacing the  
 226 term  $\left(1 - \frac{5}{3} \times D_{rel}\right)$  in Equation (4) with  $\left(1 + \frac{0.5}{6} - \frac{5}{3} \times D_{rel}\right)$ . This modification shifts the density at  
 227 which the densification rate becomes relative zero from 0.6 to 0.65 and suppresses the model  
 228 instability.

229

230 We also examine the effect of temperature on the first-stage densification mechanism and on the  
 231 critical density. Alley (1987) calculated an activation energy of 41 kJ/mol, consistent with  
 232 recommended values for grain-boundary diffusion (42 kJ/mol) or measured from grain growth rate  
 233 (Alley, 1987 and references therein). In Goujon et al. (2003), no explicit temperature effect is used  
 234 but the parameter  $\gamma$  varies by several orders of magnitude from site to site. The parameter  $\gamma$  is  
 235 calculated to maintain a continuous densification rate between the first and second stages at a  
 236 chosen critical density. We translate the variations of  $\gamma$  from site to site in to a mean activation  
 237 energy using a classical logarithmic plot as a function of  $1000/T$  (see e.g. Herron and Langway, 1980)  
 238 and obtain a value of 48 kJ/mol. Using the revised temperature dependency for the firn densification  
 239 mechanism (see next section), a slightly higher value of  $Q = 49.5$  kJ/mol is calculated (Supplementary  
 240 Figure S1). This is fairly similar to the values in Alley (1987) but much higher than the value in the  
 241 upper firn of the Herron and Langway (1980) model: 10.16 kJ/mol. Incorporating this explicit  
 242 temperature dependency term, we obtain our new final expression for the upper firn densification  
 243 rate:

244

$$245 \quad \frac{dD_{rel}}{dt} = \gamma' \left( \frac{\max(P, 0.1 \text{ bar})}{D_{rel}^2} \right) \left( 1 + \frac{0.5}{6} - \frac{5}{3} \times D_{rel} \right) \times e^{\left( -\frac{Q}{RT} \right)} \quad (6)$$

246

247 where  $\gamma' \times e^{\left( -\frac{Q}{RT} \right)}$  is equivalent to  $\gamma$  in Equation (4). However  $\gamma$  varies by two orders of magnitude  
 248 as a function of temperature whereas  $\gamma'$  remains in the range from  $0.5 \cdot 10^9$  to  $2 \cdot 10^9 \text{ bar}^{-1}$ .

249 Finally, the temperature dependency of the critical density, which defines the boundary between  
 250 the first and second stage densification mechanisms, is also re-evaluated. According to Benson  
 251 (1960) and Arnaud (1997; 2000), this critical density increases with temperature. However the slope



252 change in density profiles associated with the critical density may be difficult to locate and the  
253 Benson (1960) and Arnaud (1997) parameterizations are based on only few observation sites. We  
254 evaluate the critical density values which allow the best match of density data by our model results  
255 at 21 sites and do not find any correlation between critical density and temperature or accumulation  
256 rate (Supplementary Figure S2). We thus remove this dependency with temperature included in the  
257 old version of the LGGE model and use a mean relative critical density of 0.56 at the boundary  
258 between the first and second stage of densification in the new version of the model.

259  
260 These modifications in the formulation of the Alley (1987) mechanism improve the LGGE model  
261 stability and consistency with measured density profiles. However, when the model is run on longer  
262 timescales, only small changes of the model behaviour on glacial-interglacial transitions are  
263 observed because the first stage of densification applies to a maximal 15 m depth interval compared  
264 to the second stage (Supplementary Figure S3).

265

## 266 2.2 Densification of firn

267

268 At this stage, the observation of density profiles with depth suggests that the densification rate is  
269 controlled by a classical power law creep as used for ice deformation (Arzt et al., 1983; Maeno and  
270 Ebinuma, 1983; Wilkinson and Ashby, 1975). Arzt (1982) proposed a pressure sintering mechanism  
271 for firn densification following a power law creep and taking into account the progressive increase  
272 of the coordination number. He solved the geometrical problem of compressing a random dense  
273 packing of monosized spheres with associated deformation of each sphere into irregular polyhedra.  
274 Equation (23) of Arzt (1982) is directly used in the firn densification model.

275

### 276 2.2.1 2.2.1 Revised temperature sensitivity of the firn densification rate

277

278 A strong assumption in the firn densification module is the constant activation energy corresponding  
279 to self-diffusion of ice (60 kJ/mol). This choice corresponds to a unique mechanism supposed to  
280 drive densification. Densification is thus assumed to be driven by dislocation creep (Ebinuma and  
281 Maeno, 1987) in which the associated mechanism is lattice diffusion or self-diffusion. At the grain  
282 scale, we can describe the lattice diffusion processes associated with dislocation as diffusion within  
283 the grain volume of a water molecule from a dislocation site in the ice lattice to the grain neck in  
284 order to decrease the energy associated with grain boundaries (Blackford, 2007). Typically, an



285 activation energy of 60 to 70 kJ/mol is associated with this mechanism (Pimienta and Duval, 1987;  
286 Ramseier, 1967 and references therein).

287

288 However, multiple studies have already shown that several (6 or more) mechanisms can act  
289 together for firn or ceramic sintering (Bernache-Assollant and Bonnet, 2005; Blackford, 2007;  
290 Maeno and Ebinuma, 1983; Wilkinson and Ashby, 1975): lattice diffusion from dislocations, grain  
291 surfaces or grain boundaries; vapour transport; or surface and boundary diffusions. In order to  
292 properly take these different mechanisms into account, different activation energies (one activation  
293 energy per mechanism) should ideally be introduced in the firn densification model. Actually, it has  
294 been observed that, at warm temperature, an activation energy significantly higher than 60 kJ/mol  
295 should be favoured (up to 100-130 kJ/mol) in order to best fit density profiles with firn densification  
296 models (Arthern et al., 2010; Barnes et al., 1971; Jacka and Li, 1994). This suggests that a mechanism  
297 different from lattice diffusion is dominant for grain compaction at high temperature (i.e. higher  
298 than -10°C). At low temperature (-50°C), we are not aware of any ice sintering experiments aimed  
299 at determining the associated dominant mechanisms and activation energy. Still, by analogy with  
300 ceramic sintering, lattice diffusion from the surface of the grains should be favoured at low  
301 temperature (Bernache-Assollant and Bonnet, 2005).

302

303 Following these arguments, we propose a new parameterization of the activation energy in the  
304 LGGE firn densification model. We have thus introduced three different activation energies for the  
305 three different mechanisms highlighted above (Table 1, Figure 2). We have replaced the creep  
306 parameter in Equation (3) by:

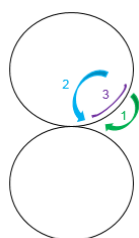
307

$$308 \quad A = A_0 \times \left( a_1 \times e^{\frac{-Q_1}{RT}} + a_2 \times e^{\frac{-Q_2}{RT}} + a_3 \times e^{\frac{-Q_3}{RT}} \right) \quad (7)$$

309

310 The parameters  $Q_1$ ,  $Q_2$  and  $Q_3$  are associated with three different firn sintering mechanisms (Figure  
311 2). We have chosen a minimal number of mechanisms (3) for simplicity in the following but the  
312 conclusions of our work would not be affected by a choice of more mechanisms.

313



- Close to melting temperature: mass transfer by vapour diffusion  
(1) mechanism 1 associated with activation energy  $Q_1$
- Low temperature: lattice diffusion (classical mechanism)  
(2) mechanism 2 associated with activation energy  $Q_2$
- Very low temperature : superficial diffusion  
(3) mechanism 3 associated with activation energy  $Q_3$

314

315 *Figure 2: Sintering mechanisms of snow by analogy with the hot ceramic sintering (inspired by Figure 8 in*  
 316 *Bernache-Assollant and Bonnet, 2005)*

317

318 The determination of  $Q_1$ ,  $Q_2$  and  $Q_3$  on the one side and  $a_1$ ,  $a_2$  and  $a_3$  on the other side are not  
 319 independent from each other. We first determine three temperature ranges corresponding to the  
 320 dominant mechanisms: vapour diffusion close to melting temperature, volume lattice diffusion due  
 321 to dislocation for low temperature and surface lattice diffusion for very low temperature. Then, we  
 322 attribute values to the activation energies  $Q_1$ ,  $Q_2$  and  $Q_3$ . The coefficients  $a_1$ ,  $a_2$  and  $a_3$  are then  
 323 adjusted to produce the expected evolution of the creep parameter with temperature (Section 3.2)  
 324 and respect the firn density profiles available (Section 3.1).

325 Our choice for the values of the different activation energies ( $Q_i$ ) is based as much as possible on  
 326 available data. For volume diffusion, several experimental determinations suggest a value for  $Q_2$   
 327 between 60 and 75 kJ/mol (Arthern et al., 2010; Barnes et al., 1971; Pimienta and Duval, 1987). For  
 328 vapour diffusion at warm temperature, empirical determinations of  $Q_1$  lead to values of the order  
 329 of 100-130 kJ/mol (Arthern et al., 2010; Barnes et al., 1971; Zwally and Li, 2002). For superficial  
 330 diffusion dominant at very low temperature, the compaction rates are too slow to be tested in a  
 331 laboratory setting, or observed in the field. As a result, we explored a large range of values for  $Q_3$ .

332 The optimal combination of  $Q_1$ ,  $Q_2$  and  $Q_3$  values (Table 1) was chosen to 1) minimize the mismatch  
 333 between modelled and measured modern density profiles, and 2) reproduce the change in LID  
 334 obtained from the  $\delta^{15}\text{N}$  data over the deglaciation at 4 Antarctic and Greenland sites (see Section  
 335 3.2 for the optimization and associated sensitivity experiments).

336 The resulting expression for the creep parameter  $A$  (Equation 7), does not significantly differ from  
 337 using simply  $A = A_0 \times e^{\left(-\frac{60000}{RT}\right)}$ , as used in the original model. To illustrate this point, we calculated

338 an equivalent activation energy,  $Q_{eq}$ , such that  $A = A_0 \times e^{\left(-\frac{Q_{eq}(T)}{RT}\right)}$ , and found  $Q_{eq}$  varying between  
 339 54 and 61 kJ/mol (Supplementary Figure S4). Thus only slight changes to the densification equation  
 340 are needed to improve the behaviour of the model at cold temperature.

341



Activation Energy (J/mol)	Coefficient
$Q_1= 110000$	$a_1= 1.05*10^9$
$Q_2= 75000$	$a_2= 1400$
$Q_3= 1500$	$a_3= 6.0*10^{-15}$

342

343 *Table 1: Preferred set of values for the three activation energies and associated pre-exponential constants*

344

345 2.2.2 2.2.2 Sensitivity of the firn densification rate to impurities

346 2.2.3

347 Firn densification can be influenced by impurity content in snow. Alley (1987) already suggested  
 348 that grain growth is influenced by impurities dissolved in ice, and that impurities in the grain  
 349 boundaries affect the relative movement of snow grains. More recently, Hörhold et al. (2012)  
 350 observed a correlation between the small scale variability of density and calcium concentration in  
 351 Greenland and Antarctic firn cores. Based on this observation, Freitag et al. (2013) proposed that  
 352 the densification rate depends on the impurity content. They implemented an impurity  
 353 parameterization in two widely used densification models (Herron and Langway, 1980; Barnola et  
 354 al., 1991), and were able to reproduce the density variability in two firn cores from Greenland and  
 355 Antarctica.

356

357 We have implemented this parameterization in our model assuming that the impurity effect is the  
 358 same for all mechanisms. Concretely, we start again from the evolution of the creep parameter with  
 359 respect to temperature given in Equation (7) and add a dependency to calcium concentration such  
 360 as:

361

$$362 \text{ if } [Ca^{2+}] > [Ca^{2+}]_{crit} : Q' = f_1 \left[ 1 - \beta \ln \left( \frac{[Ca^{2+}]}{[Ca^{2+}]_{crit}} \right) \right] \times Q \quad (8)$$

$$363 \text{ if } [Ca^{2+}] < [Ca^{2+}]_{crit} : Q' = f_1 \times Q \quad (9)$$

364

365 With,  $[Ca^{2+}]_{crit} = 0.5$  ng/g (the detection limit of continuous flow analysis).  $Q'$  represents the new  
 366 activation energy calculated in function of the calcium concentration for each site. Our main  
 367 simulations are performed with the  $f_1$  and  $\beta$  calculated by Freitag et al. (2013) for application within  
 368 the Herron and Langway model:  $f_1 = 1.025$ ,  $\beta = 0.01$ . Using the values for application within the  
 369 Pimienta-Barnola model ( $f_1 = 1.015$ ,  $\beta = 0.0105$ ) leads to similar results (section 3.2). For a first  
 370 evaluation of the impurity effect in our model, both the temperature and impurity effects are



371 combined through the application of Equations (8) and (9) to each of the three different activation  
372 energies  $Q_1$ ,  $Q_2$  and  $Q_3$ .

373

374 2.3 Densification of ice

375

376 The final stage begins at the close-off density  $\rho_{CO}$ , i.e. the density at which the average pressure in  
377 bubble starts to become higher than atmospheric pressure (Martinerie et al., 1992, Appendix 1).  
378 This density is calculated using the temperature dependent close-off pore volume given by  
379 Martinerie et al. (1994). Further densification of this bubbly ice is driven by the pressure difference  
380 between ice matrix and the air in bubbles (Maeno and Ebinuma, 1983; Pimienta, 1987). The  
381 densification rate strongly decreases with depth as these two opposite pressures tend to balance  
382 each other (Goujon et al., 2003). This stage is not essential for this study since  $\delta^{15}N$  entrapped in air  
383 bubbles does not evolve anymore.

384

385 2.4 Lock-in depth

386

387 In the previous version of the model, the LID is computed as a defined steady closed to total porosity  
388 ratio. The ratio value used can be adjusted for each drilling site, for example it is 21% for Vostok and  
389 13% at Summit in Goujon et al. (2003).

390

391 We revised the LID definition, taking into account recent advances in gas transport modelling  
392 (Wittrant et al., 2012) that allowed correct simulation of the  $\delta^{15}N$  behaviour in deep firn.  
393 Observations of modern firn air profiles show that the thickness of the lock-in zone (the zone in the  
394 deep firn with constant  $\delta^{15}N$ ) increases when the snow accumulation rate increases (Wittrant et al.,  
395 2012). Because  $\delta^{15}N$  profiles are not available for all polar firn study, we propose a new definition  
396 of the LID based on the  $\delta^{15}N$  modelling of Wittrant et al. (2012). We estimate  $\delta^{15}N$  in ice, i.e. after  
397 complete bubble closure, at 12 firn air pumping sites with the Wittrant et al. (2012) model. For each  
398 site, the trapping density ( $\rho_{LID}$ ) is then defined as the density at which the modelled  $\delta^{15}N$  value in  
399 the open porosity of the firn equals the modelled  $\delta^{15}N$  in ice. The resulting trapping density is  
400 strongly related to the accumulation rate (Supplementary Figure S5). As a result, we parameterized  
401 the trapping density ( $\rho_{LID}$ ) as a function of the accumulation rate, following:

402

$$403 \rho_{LID} = 1.43 * 10^{-2} \times \ln\left(\frac{1}{A_c}\right) + 0.783 \quad (10)$$



404

405 This parameterization leads to a much better agreement of the modelled LID with  $\delta^{15}\text{N}$  measured  
406 at the available firn sampling sites than when using the outputs of the old model. However, when  
407 used for simulating the LID during glacial periods with extremely low accumulation rate, it can  
408 predict a trapping density that is higher than the close-off density, which is unrealistic. We thus also  
409 added a threshold in our new definition of the trapping density: when  $\rho_{\text{LID}}$  exceeds the close-off  
410 density ( $\rho_{\text{CO}}$ , Section 2.3), we impose  $\rho_{\text{LID}}$  to be equal to  $\rho_{\text{CO}}$ .

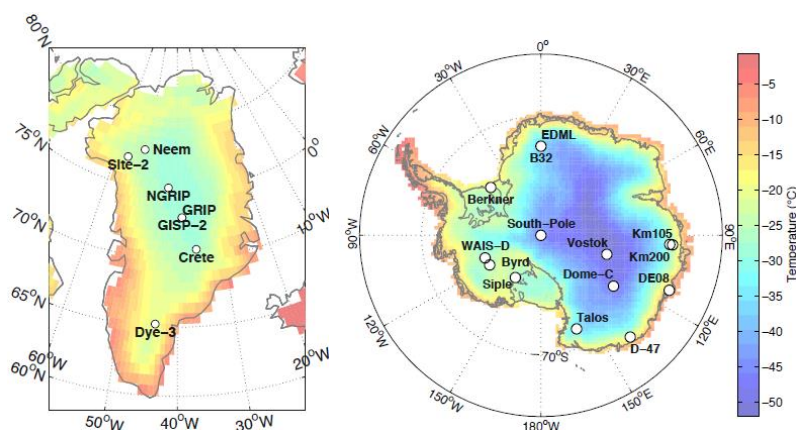
411

412 As mentioned above, this choice clearly improves the simulated  $\delta^{15}\text{N}$  in ice, at least for present-day  
413 conditions. However, this modification does not solve the strong data – model mismatch over  
414 deglaciations (Supplementary Figure S6).

415

### 416 3. Results

417



418

419

420 *Figure 3: Maps of Greenland and Antarctica showing field sites and mean annual temperature from ERA*  
421 *interim (Dee et al., 2011)*

422

#### 423 3.1 Firn density profiles

424 We assessed the behaviour of the model by comparing measured and modelled firn density profiles  
425 from 21 sites from Greenland and Antarctica (Figure 3). Figure 4 shows this comparison at Byrd,  
426 NEEM, Dome C and Vostok, and other sites are displayed in the supplement (Supplementary Figure  
427 S7). A polynomial fit was adjusted to the density data in order to facilitate the comparison with



428 model results. The data dispersion around the fit can be due natural density variations and/or  
429 measurement uncertainties.

430

431 A comparison of snow density measurement methodologies concluded that uncertainties are about  
432 10 % (Proksch et al., 2016). Moreover, although firn density profiles are often used, the  
433 measurement technique is not always well documented. Efforts were made in this study to mention  
434 the methodology when available (Supplementary Table S1). At high densities (below bubble closure  
435 depth), the hydrostatic weighing technique is expected to be about 10 times more precise than  
436 simple volume and mass measurements (Gow, 1968) but rarely used, although it is important to  
437 correctly evaluate the fairly small density difference with pure ice density. We should note that the  
438 agreement between our model results and data is good at high densities for the three sites where  
439 hydrostatic weighing technique was used: Site 2 and D-47 (Supplementary Figure S7) as well as Byrd  
440 (Figure 4).

441

442 High-resolution measurements on small samples often aim at documenting the natural variability  
443 of density. Our model only simulates bulk density, and to illustrate a meaningful comparison, the  
444 highest resolution data (at DE08, B29, B32 and Dome C) were averaged over 0.25 m windows before  
445 being plotted. At some sites, a similar averaging was already performed before data publication (e.g.  
446 1 m averaging at Byrd and Site 2, 0.5 m averaging at Mizuho). At a large number of sites, especially  
447 deep ice core drilling sites, measurements were performed on large volume samples. Still, it should  
448 be noted that at NEEM, although large volume samples were used, the data dispersion is higher  
449 than for Byrd (Figure 4) and part of the discrepancy between the model and data may be due to the  
450 uncertainty in the data.

451

452 For our study we have gathered density data covering the whole firn depth range, for which we had  
453 confidence in the data quality and the major site characteristics (temperature, accumulation).  
454 Although the effects of uncertainties on the data and natural density variability cannot be  
455 completely separated, we evaluate the data dispersion around the polynomial fit and use it as a  
456 rough indicator of data quality:

457

$$458 \quad \sigma_{fit-data} = \sqrt{\left[ \frac{\sum_{i=1}^{N_{max}} (\rho_{fit}^i - \rho_{measured}^i)^2}{N_{max}} \right]} \quad (11)$$

459



460 where  $N_{\max}$  is the number of steps of data points,  $\rho_{\text{fit}}$  represents the regression of the density profile  
 461 and  $\rho_{\text{measured}}$  the measured density averaged on a 0.25 m window.  $\sigma_{\text{fit-data}}$  generally lies below 10.0  
 462  $\text{kg/m}^3$  (Figure 5).

463

464 The modifications of the first densification stage described in Section 2.1 mainly reduce the slope  
 465 change at the transition between the Alley (1987) and Arzt (1982) mechanisms and somewhat  
 466 reduce the mismatches between the model results and polynomial fit to the data. The temperatures  
 467 and accumulation rates at Dome C and Vostok being similar, model results at these sites are similar,  
 468 but the density data have a clearly different shape. At Vostok, a high densification rate is observed  
 469 well above the critical density of about  $550 \text{ kg/m}^3$ . One possible reason is the very different flow  
 470 regimes of the two sites, one being at a Dome summit, and the other on a flow line and subject to  
 471 a traction constraint (Lipenkov et al., 1989). This is not taken into account in our simplified 1D model.  
 472 Some density data at other sites also show no densification rate change near the critical density,  
 473 resulting in model-data mismatches (see Siple Dome, km 105, km 200, Mizuho on Supplementary  
 474 Figure S7). However the new model still shows a tendency to overestimate the snow densification  
 475 rate and then underestimate the densification rate in the firn, as shown for NEEM and Vostok on  
 476 Figure 4.

477

478 The model result changes at high densities (above about  $800 \text{ kg/m}^3$ ) are mostly due to the change  
 479 in activation energies. The clearest improvement is obtained at South Pole, although the overall  
 480 impact of using three activation energies remains small. No systematic improvement of the results  
 481 was expected from adding the effect of dust as no specific tuning of the empirical parameterization  
 482 of Freitag et al. (2013) was performed in our model, but the model results using the original  
 483 parameterization of Freitag et al. (2013) always remain in reasonable agreement with the data. This  
 484 is due to the fact that the impurity concentration remains small in modern climate, and  
 485 consequently dust has a limited effect on the creep parameter (see also Supplementary Figure S4).  
 486 In order to more quantitatively address and visualize the model data comparison with the different  
 487 versions of the model on the 21 selected sites, we calculate the following deviation in parallel to the  
 488  $\sigma_{\text{fit-data}}$  above (Equation 11):

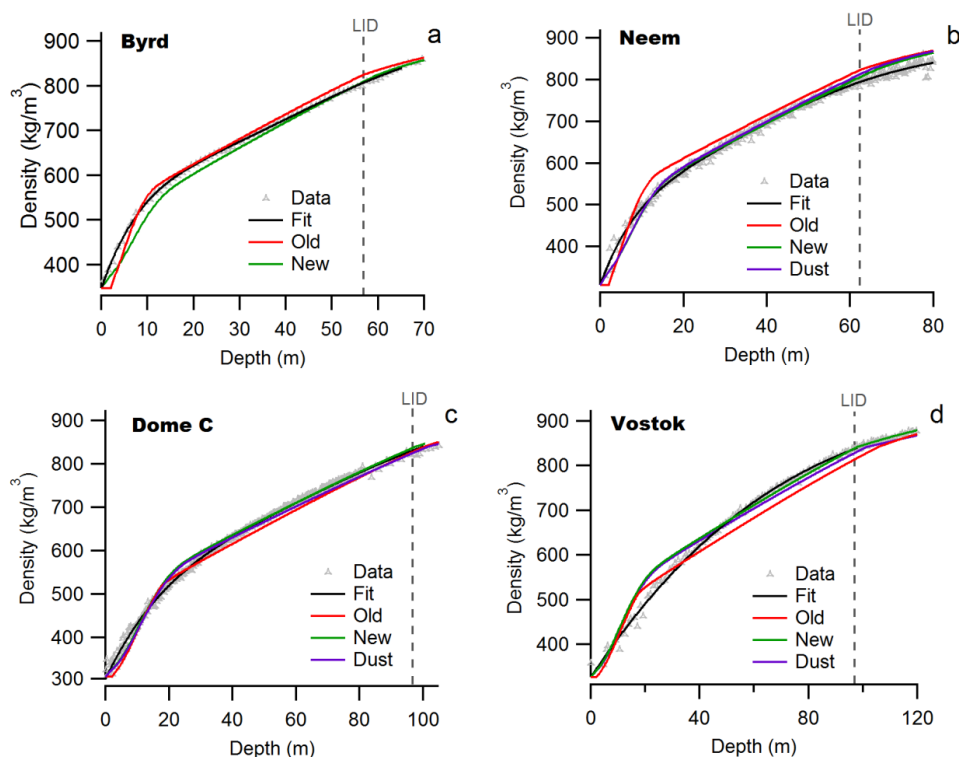
489

$$490 \quad \sigma_{\text{model-fit}} = \sqrt{\left[ \sum_{i=1}^{N_{\max}} \frac{(\rho_{\text{model}}^i - \rho_{\text{fit}}^i)^2}{N_{\max}} \right]} \quad (12)$$

491



492 Figure 5 and Supplementary Table S1 display the  $\sigma_{\text{model-fit}}$  for the 21 different sites before and after  
 493 modifications detailed in Section 2. Overall, in terms of  $\sigma_{\text{model-fit}}$ , only a small improvement (about  
 494 3%) is obtained by using the modified model rather than the former Goujon et al. (2003) mechanical  
 495 scheme. However a systematic improvement is obtained at the five coldest sites. On the other hand,  
 496 the incorporation of the impurity effects following the Freitag et al. (2013) parameterization in our  
 497 model most often deteriorates the model-data agreement.  
 498

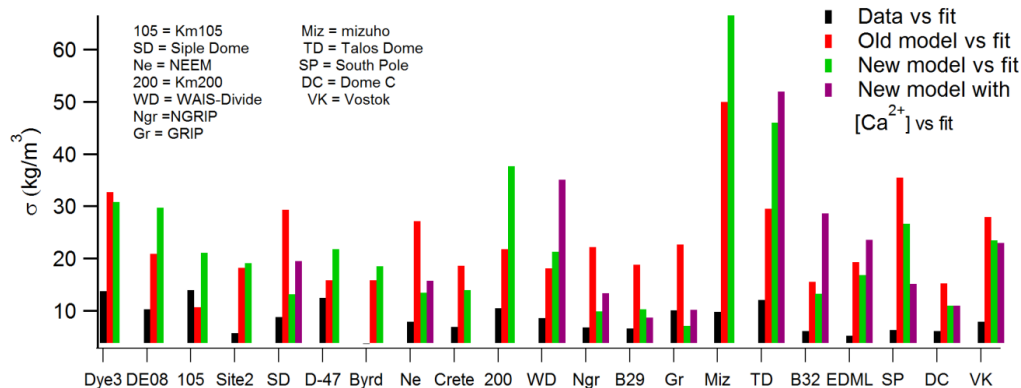


499  
 500  
 501 *Figure 4: Density profiles of Byrd (a), NEEM (b), Dome C (c) and Vostok (d). The grey triangles correspond to the data.*  
 502 *The black line corresponds to the polynomial fit, the red one to the old simulation, the green one to the new simulation*  
 503 *and the purple one to the new simulation with impurity effect.*

504  
 505 The comparison of the values of  $\sigma_{\text{model-fit}}$  with  $\sigma_{\text{fit-data}}$  shows that both are of the same order of  
 506 magnitude. This means that our new model reproduces correctly the firn density profiles at different  
 507 sites. The main disagreement between model and data is observed at the transition between the  
 508 first and the second densification stage with too high modelled densities and an associated slope  
 509 change in the density profile that is too strongly imprinted. This effect is due to a densification rate



510 that is too high in the first stage, and this formulation is not affected by the new temperature  
 511 sensitivity.  
 512  
 513 The first stage of densification is not crucial for our purpose here, which is to improve the agreement  
 514 between the modelled LID and the evolution of  $\delta^{15}\text{N}$  over deglaciations in Antarctica. In order to  
 515 evaluate the ability of the model to predict the LID, we compared the depths at which the LID  
 516 density, as defined by Equation (10), is reached in the polynomial fit to the data and in the new  
 517 model results. In the old version of the model, the LID differences between the model and data  
 518 range between -17.9 m (at South Pole) and +8.6 m (at km 200) with a small mean value of -1.9 m  
 519 and a standard deviation of 6 m. In the new version, the LID differences between the model and  
 520 data are comparable, ranging between -14.1 m (at South Pole) and +12.8 m (at Talos Dome) with a  
 521 small mean value of -0.7 m and a standard deviation of 6 m. We thus conclude from this section  
 522 that the LGGE new firn densification model preserves the good agreement between (1) modelled  
 523 and measured firn density profiles and (2) modelled and measured LID. We explore in the next  
 524 section the performances of the new model for coldest and driest conditions by looking at the  
 525 modelled LID and hence  $\delta^{15}\text{N}$  evolution over glacial – interglacial transitions.  
 526



527  
 528  
 529 *Figure 5: Representation of the  $\sigma_{fit-data}$  in black and the  $\sigma_{model-fit}$  (in red for the old model, in green for the new  
 530 model and in purple for the new model with the impurity effect) at 21 Greenland and Antarctic sites. The site  
 531 characteristics are provided in Supplementary Table S1.*

532  
 533 3.2  $\delta^{15}\text{N}$  glacial-interglacial profiles



534 In order to test the validity of the densification model in a transient mode, we model the time  
535 evolution of  $\delta^{15}\text{N}$  over the last deglaciation, and compare it to measurements at 4 Antarctic and  
536 Greenland deep ice-core sites: Dome C (cold and low accumulation site in Antarctica with a strong  
537 mismatch observed between data and the old model), EDML (intermediate temperature and  
538 accumulation rate in Antarctica with a significant mismatch between data and the old model), WAIS-  
539 Divide (high temperature and accumulation rate site in Antarctica with a good model-data  
540 agreement) and NGRIP (Greenland site with a good agreement between model and data) (Figure 3).  
541 The computation of  $\delta^{15}\text{N}$  depends on the LID and on the firn temperature profile. The gravitational  
542  $\delta^{15}\text{N}$  signal is indeed calculated from the LID and mean firn temperature according to the barometric  
543 equation (Equation 1). The thermal  $\delta^{15}\text{N}$  depends on the temperature gradient between the surface  
544 and the LID. The thermal  $\delta^{15}\text{N}$  signal remains small in Antarctica because the temperature variations  
545 are slow ( $<2^\circ\text{C}/1000$  years), and is only important for abrupt climate changes in Greenland (e.g.  
546 NGRIP).

547 3.2.1

548 3.2.2 3.2.1 Input scenarios

549

550 For the simulation of the  $\delta^{15}\text{N}$  evolution over the last deglaciation, the firn densification model is  
551 forced by a scenario of surface temperature and accumulation rate deduced from ice core data. In  
552 Greenland (NGRIP, GISP2), the temperature is reconstructed using the  $\delta^{18}\text{O}_{\text{ice}}$  profiles together with  
553 indication from borehole temperature measurements (Dahl-Jensen, 1998) and  $\delta^{15}\text{N}$  data for NGRIP  
554 (Kindler et al., 2014) for the quantitative amplitude of abrupt temperature changes. Greenland  
555 accumulation rate is deduced from layer counting over the last deglaciation (e.g. Rasmussen et al.,  
556 2006). The uncertainty in the temperature reconstructions can be estimated to  $\pm 3^\circ\text{C}$  over the last  
557 deglaciation in Greenland (Buizert et al., 2014). As for the Greenland accumulation rate, an  
558 uncertainty of 20% can be associated with the LGM value (Cuffey and Clow, 1997; Guillevic et al.,  
559 2013; Kapsner et al., 1995). In Antarctica, both temperature and accumulation rate are deduced  
560 from water isotopic records except for WAIS-Divide, where layer counting back to the last glacial  
561 period is possible (Buizert et al., 2015). Temperature uncertainty for the amplitude of the last  
562 deglaciation is estimated to -10% to +30% in Antarctica (Jouzel, 2003). In the construction of the  
563 AICC2012 chronology (Bazin et al., 2013; Veres et al., 2013), the first order estimate of accumulation  
564 rate from water isotopes for EDML, Talos Dome, Vostok and Dome C has been modified by  
565 incorporating dating constraints or stratigraphic tie points between ice cores (Bazin et al., 2013;  
566 Veres et al., 2013). The modification of the accumulation rate profiles over the last deglaciation for



567 these 4 sites is less than 20% and the uncertainty of accumulation rate generated by the DATICE  
568 model used to build AICC 2012 from background errors (thinning history, accumulation rate, LID)  
569 and chronological constraints is 30% for the LGM (Bazin et al., 2013; Frieler et al., 2015; Veres et al.,  
570 2013). These values are consistent with previous estimates of accumulation rate uncertainties over  
571 the last deglaciation ( $\pm 10\%$  for Dome C (Parrenin et al., 2007) and  $\pm 30\%$  in EDML (Loulergue et al.,  
572 2007)). The references of the scenarios for temperature and accumulation rate over the deglaciation  
573 used in this study are given in Supplementary Table S2.

574

575 We showed in Section 2.1 that surface density does not have a strong impact on the LID  
576 determination (Supplementary Figure S3). We do not have any indication of surface density in the  
577 past, so we impose a constant surface density of 0.35 for all sites at all times for transient runs. In  
578 order to convert the LID (deduced from density) to the diffusive column height measured by  $\delta^{15}\text{N}$ ,  
579 we need an estimate of the convective zone in the past. We use a 2 m convective zone for all sites,  
580 except Vostok, where we use 13 m, in accordance with firn measurements (Bender et al., 2006). We  
581 assume that the convective zone did not evolve during the last deglaciation, consistently with dating  
582 constraints at Dome C and at Vostok during Termination 2 (Parrenin et al., 2012; Bazin et al., 2013;  
583 Veres et al., 2013; Landais et al., 2013).

584

585 3.2.2 Transient run with the old model

586

587 In this section, we focus on the  $\delta^{15}\text{N}$  evolution over the deglaciation at different Greenland and  
588 Antarctic sites as obtained from the data and as modelled with the old version of the LGGE model.  
589 This comparison serves as a prerequisite for the comparison with outputs of the improved model  
590 over the same period for the same polar sites. The comparison between the old LGGE model and  
591  $\delta^{15}\text{N}$  data over the last deglaciation shows the same patterns as already discussed in Capron et al.  
592 (2013). At Greenland sites, there is an excellent agreement between model and data showing both  
593 the decrease in the mean  $\delta^{15}\text{N}$  level between the LGM and the Holocene and the  $\sim 0.1\text{‰}$  peaks in  
594  $\delta^{15}\text{N}$  associated with the abrupt temperature changes (end of the Younger Dryas, Bølling-Allerød,  
595 Dansgaard-Oeschger 2, 3 and 4, Figure 6 and Supplementary Figure S8). On the other hand, the  
596 modelled and measured  $\delta^{15}\text{N}$  over the last deglaciation show significant dissimilarities in Antarctic  
597  $\delta^{15}\text{N}$  profiles displayed on Figure 6 and Supplementary Figure S8, except at the relatively high  
598 accumulation rate and temperature site of WAIS-Divide where the model simulates properly the  
599  $\delta^{15}\text{N}$  evolution in response to the change in accumulation and mean firn temperature estimated



600 from water isotopic records and borehole temperature constraints (Buizert et al., 2015). Note that  
601 in Buizert et al. (2015), the modelled  $\delta^{15}\text{N}$  was obtained from the Herron and Langway model. For  
602 the other Antarctic sites (Figure 6), we observe that model and data disagree on the  $\delta^{15}\text{N}$  difference  
603 between the LGM and Holocene levels. At EDML, Dome C and Vostok, the model predicts a larger  
604 LID during the LGM, while  $\delta^{15}\text{N}$  suggests a smaller LID compared to the Holocene (with the  
605 assumption of no change in convective zone during the deglaciation). In addition, the measured  
606  $\delta^{15}\text{N}$  profiles at Berkner Island, Dome C, EDML and Talos Dome display an additional short term  
607 variability, i.e.  $\delta^{15}\text{N}$  variations of 0.05‰ in a few centuries during stable climatic periods. These  
608 variations can be explained by the ice quality (coexistence of bubbles and clathrates) at Dome C and  
609 EDML. Indeed, for pure clathrate ice from these two sites, such short term variability is not observed  
610 (e.g. Termination 2 at Dome C, Landais et al., 2013). At Berkner Island and Talos Dome, these  
611 variations cannot be explained by the quality of the measurements, by thermal effects nor by dust  
612 influence. They are also not present in the accumulation rate and temperature forcing scenarios  
613 deduced from water isotopes (Capron et al., 2013). This observation questions the possible  
614 presence of a convective zone and/or the accuracy of the reconstruction of past accumulation rate  
615 and temperature scenarios from water isotopes in Antarctica except at WAIS-Divide where layer  
616 counting is possible over the last deglaciation. We thus explore further the influence of  
617 accumulation rate and temperature uncertainties on the  $\delta^{15}\text{N}$  modelling.

618

619 The uncertainties in the changes of temperature and accumulation rates over the deglaciation  
620 significantly influences the simulated  $\delta^{15}\text{N}$ , as already shown in previous studies and this sensitivity  
621 of  $\delta^{15}\text{N}$  has even been used to adjust temperature and/or accumulation rate scenarios (Buizert et  
622 al., 2013; Guillevic et al., 2013; Kindler et al., 2014; Landais et al., 2006). We tested the influence of  
623 the accumulation rate and temperature scenarios on the simulated  $\delta^{15}\text{N}$  profiles for the last  
624 deglaciation, but even with large uncertainties in the input scenarios, it is not possible to reproduce  
625 the measured Antarctic  $\delta^{15}\text{N}$  increase at Dome C and EDML with the old version of the LGGE model.

626

627 This result is illustrated on Figure 7 where we display a comparison between the amplitude of the  
628 measured  $\delta^{15}\text{N}$  change and the amplitude of the modelled  $\delta^{15}\text{N}$  change with the Goujon version  
629 over the last deglaciation. For this comparison, we calculated the Last Glacial Maximum (LGM)  $\delta^{15}\text{N}$   
630 average over the period 18-23 ka and the Early Holocene (EH)  $\delta^{15}\text{N}$  average over the period 6-10 ka  
631 (or smaller, depending on available data, cf blue boxes on Figure 6). We estimated the uncertainty  
632 in the measured  $\delta^{15}\text{N}$  change by calculating first the standard deviation of the  $\delta^{15}\text{N}$  data over each



633 of the two periods, LGM and EH as  $\sigma_{15N\_data\_EH}$  and  $\sigma_{15N\_data\_LGM}$  and then the resulting uncertainty

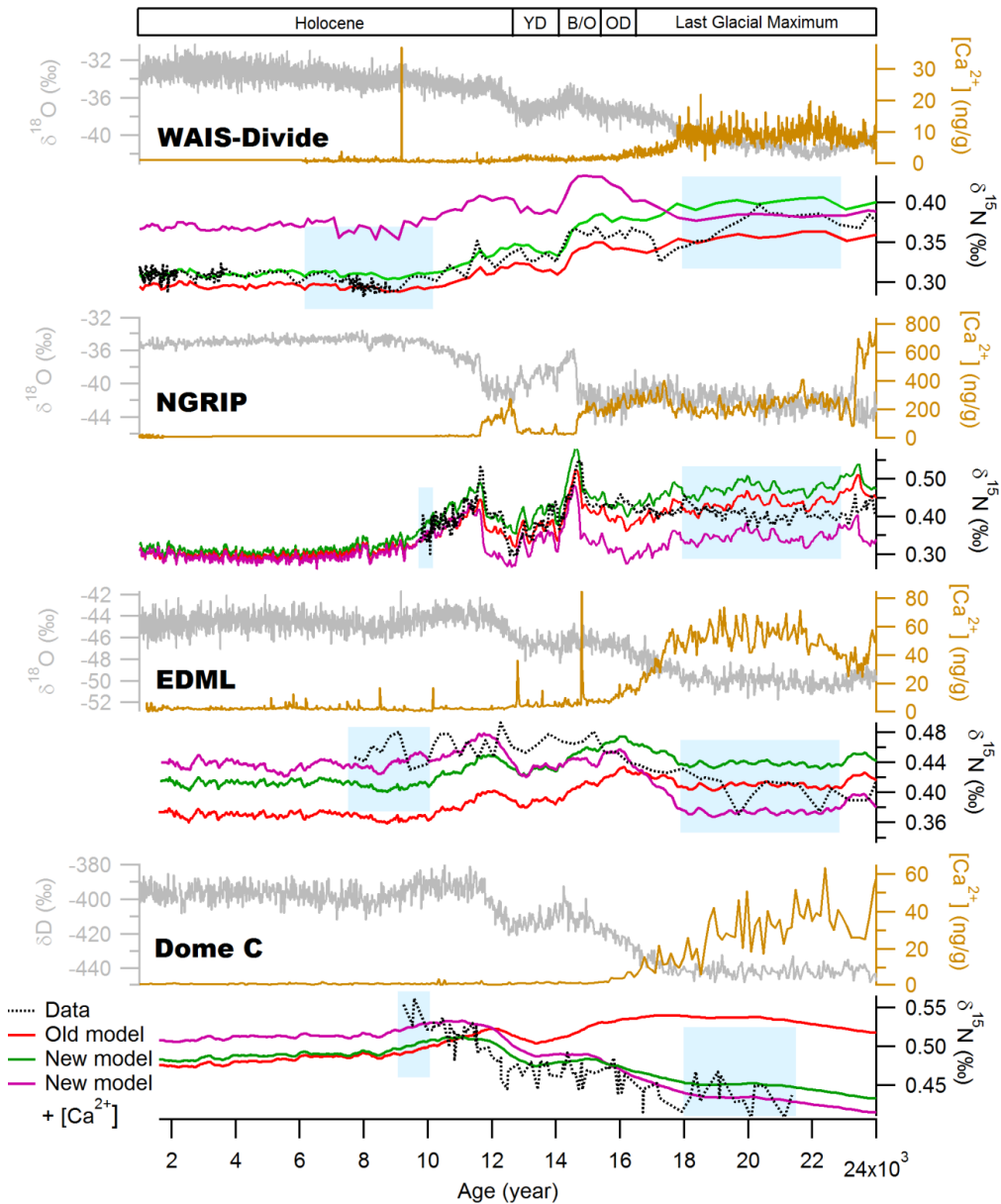
634 on the  $\delta^{15}N$  change as:

635 
$$\sigma_{15N\_EH-LGM} = \sqrt{\sigma_{15N\_data\_EH}^2 + \sigma_{15N\_data\_LGM}^2} .$$

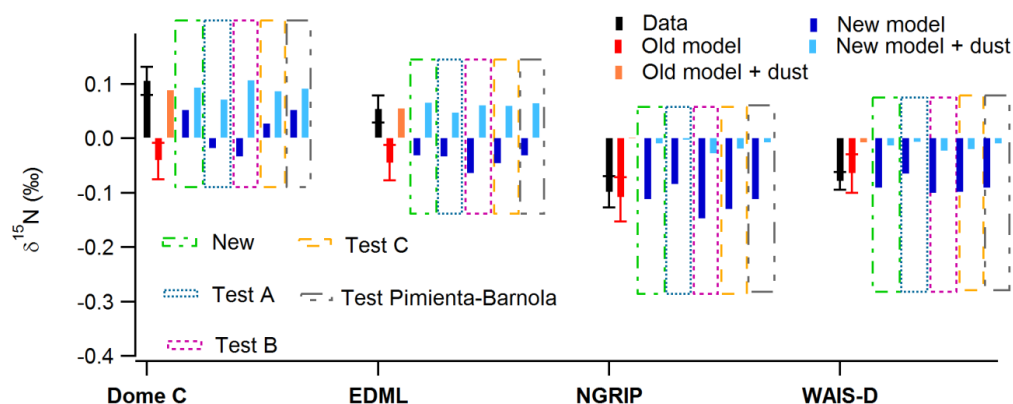
636 As for the modelled  $\delta^{15}N$  change, associated error bars are deduced from the uncertainty on the  
637 temperature and accumulation input scenarios (shown on Supplementary Figure S9 for the  
638 improved model). The total error bar hence shows the difference between most extreme  
639 accumulation rate or temperature input scenarios. In these sensitivity tests, we assumed that it is  
640 not possible to have an underestimation of the temperature change with an overestimation of the  
641 accumulation rate (or the opposite) because changes in accumulation rate and temperature are  
642 linked, at least qualitatively.

643

644



645  
 646 *Figure 6:* Comparison of the measured  $\delta^{18}\text{O}$  or  $\delta\text{D}$  (grey), the calcium concentration (gold), the measured  $\delta^{15}\text{N}$  (black)  
 647 and the modelled  $\delta^{15}\text{N}$  (old (red), new version (green) and new version with impurity (purple)) of the LGGE model for  
 648 WAIS-Divide, NGRIP, EDML and Dome C. Blue boxes for each sites indicate the periods over which the  $\delta^{15}\text{N}$  average for  
 649 the LGM and EH have been estimated for the calculation of the amplitude of the  $\delta^{15}\text{N}$  change over the deglaciation.  
 650



651

652 *Figure 7: Difference between EH and LGM  $\delta^{15}\text{N}$  at 4 different polar sites (raw data are given in Supplementary Table S3).*

653 *The measured  $\delta^{15}\text{N}$  difference is shown with a black bar. The modelled  $\delta^{15}\text{N}$  difference is shown with colours: old version*

654 *in red (orange with the impurity influence), new version in blue with different parameterizations. “New” corresponds to*

655 *the parameterization of Table 1, sensitivity tests A, B and C are explained on Table 3. When “+ dust” is mentioned, it*

656 *corresponds to the addition of the impurity influence as parameterized by Freitag et al., (2013) (Equations 8 and 9). Test*

657 *Pimienta-Barnola corresponds to a test with the Freitag parameterization adapted to the Pimienta-Barnola model*

658 *instead of the Herron and Langway model used for the other sensitivity tests. This test shows in light blue the result of*

659 *the implementation of this parameterization combined with the “New” parameterization from Table 1. The same red*

660 *error bars can be applied to all model outputs for each sites.*

661

### 662 3.2.3 Results with updated temperature parameterization

663

664 By construction, the new LGGE firn model with the temperature dependency of the firn densification

665 module depicted on Section 2.2.1 is expected to improve the agreement between model and data

666 for cold sites of East Antarctica over the last deglaciation by increasing densification rate at low

667 temperature. This new parameterization modifies the densification rate through the creep

668 parameter given in Equation (7). Figure 8 shows the evolution of the creep parameter with

669 temperature for different choices of the three activation energies  $Q_1$ ,  $Q_2$  and  $Q_3$ . Compared to the

670 old model, the densification rate is higher at low temperature, below  $-55^\circ\text{C}$  (i.e. for LGM at Dome C

671 and Vostok, Table 1). At higher temperature (between  $-55^\circ\text{C}$  and  $-28^\circ\text{C}$  corresponding to present-

672 day temperature in most polar sites), the creep parameter is slightly lower than in the old model.

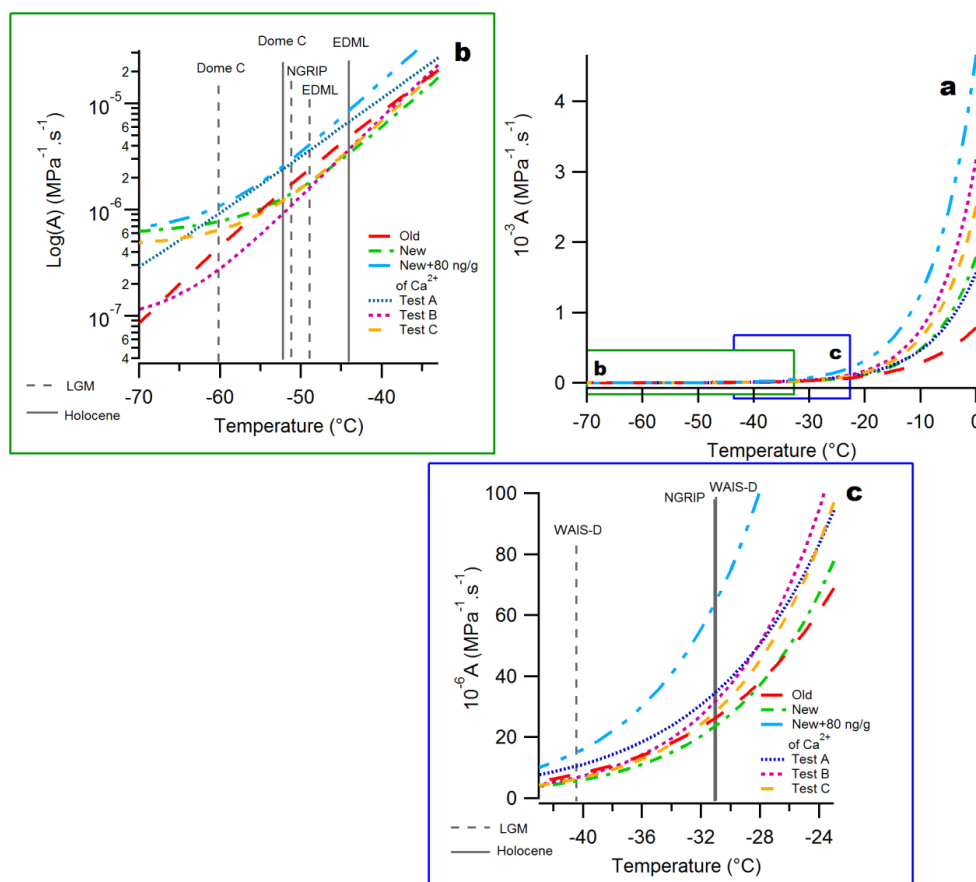
673 The difference between the 2 curves is however not large so that densification rate is not strongly

674 modified over this range. This is in agreement with comparable firn density profiles obtained for the

675 different polar sites using the old or the improved LGGE model (Section 3.1, Figure 4).



676 In the improved model, the simulated profiles of  $\delta^{15}\text{N}$  are comparable to  $\delta^{15}\text{N}$  simulated with the  
 677 old model at the sites that were already showing a good agreement between the old model outputs  
 678 and data, for example NGRIP, GISP-2, Talos Dome and WAIS-Divide (Figure 6 and Supplementary  
 679 Figure S8). This is expected since the corresponding densification rate is only slightly reduced in the  
 680 temperature range of  $-55^\circ\text{C}/-28^\circ\text{C}$  which corresponds to the temperature range encompassed over  
 681 the last deglaciation at these sites. This results in a deeper LID and hence higher  $\delta^{15}\text{N}$  level, which is  
 682 in general compatible with the data. At the coldest sites (Dome C, Vostok), the agreement between  
 683 data and modelled profiles is largely improved with a modelled LGM  $\delta^{15}\text{N}$  smaller than the modelled  
 684 EH  $\delta^{15}\text{N}$ , but a perfect match cannot be found. At the intermediate EDML site, it is not possible to  
 685 reproduce the sign of the slope during the deglaciation.  
 686



687  
 688  
 689 *Figure 8: Evolution of the creep parameter (Equation 7) as a function of temperature for 6 different*  
 690 *parameterizations. “Old” corresponds to the Goujon et al. (2003) version of the model; “New” corresponds to*



691 *the improved LGGE model with parameterization described in Table 1; “New + 80 ng/g of Ca<sup>2+</sup>” corresponds*  
 692 *to the parameterization of Table 1 with the addition of the impurity effect following Equation (8) and a [Ca<sup>2+</sup>]*  
 693 *value of 80 ng/g; Tests A, B and C are sensitivity tests run with the values presented on Table 3. Figure 8a*  
 694 *shows the creep parameter evolution for the whole temperature range, Figure 8b is a focus at very low*  
 695 *temperature and Figure 8c is a focus at intermediate temperature. The grey vertical lines indicates the*  
 696 *temperature for Early Holocene (EH, solid line) and LGM (dotted line) at the 4 study sites presented in Figures*  
 697 *6 and 7.*  
 698

Test	Activation energy (J/mol)	Coefficient
Test A	90000	5.5*10 <sup>5</sup>
	60000	1.0
	30000	4.5*10 <sup>-8</sup>
Test B	110000	5.5*10 <sup>9</sup>
	75000	1950.0
	1500	9.0*10 <sup>-16</sup>
Test C	100000	4.5*10 <sup>7</sup>
	75000	1670.0
	1500	4.6*10 <sup>-15</sup>

699  
 700 *Table 3: Values used for the different sensitivity tests for three activation energies.*  
 701

702 In order to more quantitatively assess the robustness of the proposed parameterization in Table 1,  
 703 we confront in Figure 7 the measured and modelled  $\delta^{15}\text{N}$  differences between the LGM and EH at  
 704 the 4 Greenland and Antarctic sites selected above. For this comparison, we use not only the  
 705 parameterization of Table 1 but also sensitivity tests performed with different parameterizations of  
 706 the temperature dependency of activation energy and impurity effects (details on Table 3). When  
 707 using the parameterization of Table 1 (“new model”), Figure 7 shows strong improvement of the  
 708 agreement between measured versus modelled  $\delta^{15}\text{N}$  difference between EH and LGM with, as  
 709 mentioned above and shown on Figure 6, an inversion of the  $\delta^{15}\text{N}$  difference for the very cold sites  
 710 of East Antarctica (Figure 7).

711 The sensitivity tests illustrate the choice of our final parameterization. As displayed in Figure 8, test  
 712 A has a higher creep parameter than the old model throughout the whole temperature range.  
 713 Compared to the output of the old model, the LGM vs EH  $\delta^{15}\text{N}$  change simulated with test A is slightly  
 714 higher but the sign of the  $\delta^{15}\text{N}$  change over the last deglaciation is still wrong at Dome C and EDML.  
 715 This test shows that it is not the mean value of the creep parameter that needs to be changed, but  
 716 the dependency to temperature. Test B has a higher creep parameter above -35°C, but a lower creep



717 parameter than the old model below  $-35^{\circ}\text{C}$ , which starts flattening and hence reaching values higher  
718 than the old model creep parameter below  $-65^{\circ}\text{C}$ . The LGM vs EH  $\delta^{15}\text{N}$  change simulated with test  
719 B is still comparable with data at WAIS-Divide. However, the model – data comparison deteriorates  
720 at NGRIP and EDML compared to the model-data comparison with the old version of the model.  
721 Moreover, it does not solve the model – data mismatch at Dome C. This shows that the change in  
722 the creep parameter at intermediate temperature is too steep. Test C is rather close to the “new  
723 model” over most of the temperature range. Strong differences occur at high temperature (above -  
724  $30^{\circ}\text{C}$ ) but it does not affect the modelled  $\delta^{15}\text{N}$  change between LGM and EH for our 4 sites. On the  
725 contrary, the slightly lower creep parameter at low temperature leads to a less good agreement  
726 between model and data for the Dome C deglaciation than when using the “new model”.

727

728 Summarizing, the best agreement between data and model for Dome C is obtained for the  
729 parameters given on Table 1: the creep parameter of “new model” flattens below  $-50^{\circ}\text{C}$  and is thus  
730 not very different for the LGM or the EH at Dome C. As a result, the modelled LID and hence  $\delta^{15}\text{N}$   
731 are less sensitive to temperature, and the sign of the EH-LGM difference can be inverted, and  
732 brought closer to the observations. It should be noted that despite many sensitivity tests we could  
733 not find a parameterization able to reproduce the EH-LGM  $\delta^{15}\text{N}$  changes for all 4 sites. In the “new  
734 model” without impurity effect, it is not possible to reproduce the measured EDML  $\delta^{15}\text{N}$  change  
735 over the last deglaciation even when taking into account the uncertainty in the input parameters  
736 (temperature and accumulation rate, Supplementary Figure S9).

737

#### 738 3.2.4 Impurity softening

739

740 The dust content in LGM ice is much larger than in Holocene ice (Figure 6), and impurity inclusions  
741 in ice have an impact on the grain structure, allowing it to deform more easily (Alley, 1987; Fujita et  
742 al., 2014). We incorporated dust softening using the parameterization of Freitag et al (2013) as  
743 detailed in Section 2.2.2. We compared two expressions for the impurity softening (tuned to be  
744 applied to the Herron and Langway model, or Pimienta and Barnola model), but found that the  
745 differences between the two parameterisations were minor (Figure 7). We use the Herron and  
746 Langway parameters in the following.

747

748 Figure 8 shows the effect of impurities on the creep parameter: densification is enhanced over the  
749 whole temperature range. At all sites, incorporating impurity softening reduces the firn thickness



750 during periods characterized by high impurity concentration in the ice (LGM). It thus leads to an  
751 increase of the EH-LGM LID difference (Figure 7).

752

753 This effect clearly helps to bring in agreement modelled and measured  $\delta^{15}\text{N}$  at Dome C, Vostok and  
754 EDML (Figures 6, 7 and Supplementary Figure S8): for these sites, the model incorporating the  
755 parameterization of activation energy depicted in Table 1 and the impurity effects is able to  
756 reproduce the  $\delta^{15}\text{N}$  increase over the last deglaciation. Note that short-lived peaks in impurities,  
757 likely triggered by volcanic events, have a limited effect on bulk firn thickness (Figure 6). Contrary  
758 to the improved situation in cold Antarctic sites, we observe that, at the warmer sites like NGRIP  
759 and WAIS-Divide, incorporating impurity softening deteriorates the model data fit, which was  
760 already good in the older version of the model, and also good with other firn densification models  
761 (Kindler et al, 2014; Buizert et al, 2015). It produces almost no change in firn thickness between the  
762 LGM and the EH at NGRIP, which contradicts  $\delta^{15}\text{N}$  observations. The same mismatch is observed at  
763 WAIS-Divide using a different model, as already noted by Buizert et al. (2015). We tested the  
764 sensitivity to the dust parameterization by implementing the Freitag parameterization adapted to  
765 the Pimienta-Barnola model instead of the Herron and Langway model used with our improved  
766 model (cf section 2.2.2). The two different parameterizations of the impurity effect lead to very  
767 comparable LGM to EH  $\delta^{15}\text{N}$  changes over the last deglaciation on the 4 sites discussed here.

768

769 The mismatch observed for the  $\delta^{15}\text{N}$  simulations at WAIS-Divide and NGRIP when incorporating the  
770 impurity effect suggests that the parameterization presented in Equations (8) and (9) is not  
771 appropriate to be used on bulk  $[\text{Ca}^{2+}]$  concentration and/or for LGM simulation. Actually, the  
772 proposed parameterization by Freitag et al. (2013) was tuned to density variability in present-day  
773 firn, and may not be valid for LGM when  $[\text{Ca}^{2+}]$  concentrations were 10-100 times larger than  
774 present-day. It is also possible that the dust effect saturates at high concentration, and is no longer  
775 sensitive above a certain threshold.

776

777 It is also possible that impurity influence, like temperature, acts differently depending on the  
778 dominant mechanism for firn deformation, and that the impurity effect is more important at colder  
779 temperature. The mechanisms by which impurities influence firn deformation are still poorly  
780 understood. In particular, the solubility of dust particles, and their position inside or at the grain  
781 boundaries may act on deformation in opposite way. More work is thus needed before the correct  
782 “impurity effect” component and the mechanisms by which it acts on densification are identified



783 (e.g. Fujita et al., 2014, 2016). Here, we have shown that a simple parameterization as a function of  
784  $[Ca^{2+}]$  concentration does not provide uniformly good results, and seems only suitable for sites on  
785 the Antarctic Plateau.

786

787 To sum up, the new parameterization of the creep parameter preserves good agreement between  
788 the old model outputs and data at sites that were already well simulated (WAIS-Divide, NGRIP, Talos  
789 Dome), and improves the simulation of the deglaciation at cold Antarctic Sites (Dome C, Vostok).  
790 However, the EH-LGM  $\delta^{15}N$  change at Dome C and EDML cannot be reproduced using only the  
791 temperature dependency of activation energy. The inclusion of impurity effect improves the  
792 situation for cold sites but leads to inconsistent  $\delta^{15}N$  evolutions over the deglaciation at WAIS-Divide  
793 and NGRIP.

794

#### 795 4. Conclusion and perspectives

796

797 In this study, we have presented an up-to-date version of the LGGE firn densification model. We  
798 have summarized the physical basis and parameterization choices of this firn model that would  
799 explain the disagreement between model and data on both the firn density profiles and the  $\delta^{15}N$   
800 evolution over the last deglaciation. The mismatch was particularly strong in the extremely cold sites  
801 of East Antarctica where modelled  $\delta^{15}N$  shows an increase over the deglaciation, contrary to the  
802 measured  $\delta^{15}N$  decrease. Based on analogy with ceramic sintering at hot temperature and recent  
803 observations of the impurity effect on firn density, we have improved the LGGE densification model  
804 by incorporating new parameterizations for the evolution of the creep parameter with temperature  
805 and impurity contents within the firn densification module. We follow previous studies evidencing  
806 different dominant firn sintering mechanisms in different temperature ranges that support a  
807 temperature dependency of the creep activation energy. We showed that these new  
808 parameterizations improve the agreement between model and data at low temperature (below -  
809  $30^{\circ}C$ ), and retain the good agreement at warmer temperature. In particular, the improved LGGE firn  
810 density model is now the first firnification model able to reproduce the  $\delta^{15}N$  increase over  
811 deglaciations at cold sites such as Dome C and Vostok.

812

813 The new parameterization implies a more rapid firn densification at lower temperature and high  
814 impurity load than in classical firnification models. This leads to a significantly lower  $\Delta age$  in glacial  
815 period for deep polar ice cores such as Dome C, Vostok and Dome Fuji. This result is in agreement  
816 with the recent low  $\Delta age$  estimate by Parrenin et al. (2012) over the deglaciation at Dome C. This



817 has important consequences for the study of the CO<sub>2</sub> vs Antarctic temperature lead or lag over  
818 deglaciation. Our new parameterization is hence in agreement with the recent study of Parrenin et  
819 al. (2013) showing that the increases in East Antarctic temperature and CO<sub>2</sub> are synchronous over  
820 the last deglaciation.

821

822 The new parameterization proposed here calls for further studies. First, laboratory or field studies  
823 of firn densification at very cold controlled conditions would ideally be needed to check the  
824 predominance of the surface lattice diffusion mechanism around -60°C; this is a real challenge  
825 because of the slow speed of deformation. Second, we have suggested that the current  
826 parameterization of impurity on firn softening should be revised for glacial conditions with low  
827 temperature (Greenland) and very high impurity load. Third, the separate effects of impurities and  
828 temperature on firn densification and hence  $\delta^{15}\text{N}$  evolution should be tested on different periods  
829 than the last deglaciation. Sequences of events associated with non-synchronous changes in surface  
830 temperature, accumulation rate and impurity content would be particularly valuable for this  
831 objective.

832

833 *Acknowledgements:* We thank Anders Svensson, Rob Arthern and Hans Christian Steen-Larsen for  
834 data sharing and Sarah Guilbaud for her work during her final internship study. Thanks to Pierre  
835 Badel for insightful discussions about densification mechanisms. Thanks to Myriam Guillevic for her  
836 work on the densification model and helpful discussions. This work is supported by INSU/CNRS LEFE  
837 project NEVE-CLIMAT.

838

839



840 References

841

842 Alley, R. B.: Firn densification by grain-boundary sliding: a first model, *J. Phys. Colloq.*, 48(C1), C1-  
843 249-C1-256, doi:10.1051/jphyscol:1987135, 1987.

844 Anderson, D. L. and Benson, C. S.: The densification and diagenesis of snow, in *Ice and Snow: Properties, Processes and Applications*, pp. 391–411, MIT Press., 1963.

846 Arnaud, L.: Modélisation de la transformation de la neige en glace à la surface des calottes polaires;  
847 Etude du transport des gaz dans ces milieux poreux, PhD Thesis, Université Joseph Fournier -  
848 Grenoble 1, 294 pp, 1997.

849 Arnaud, L., Barnola, J. M. and Duval, P.: Physical modeling of the densification of snow/firn and ice  
850 in, *Phys. Ice Ore Rec.*, 26, 39–44, 2000.

851 Arthern, R. J., Vaughan, D. G., Rankin, A. M., Mulvaney, R. and Thomas, E. R.: In situ measurements  
852 of Antarctic snow compaction compared with predictions of models, *J. Geophys. Res.*, 115(F3),  
853 doi:10.1029/2009JF001306, 2010.

854 Arzt, E.: The influence of an increasing particle coordination on the densification of spherical  
855 powders, *Acta Metall.*, 30(10), 1883–1890, 1982.

856 Arzt, E., Ashby, M. F. and Easterling, K. E.: Practical applications of hot-isostatic pressing diagrams:  
857 four case studies, *Metall. Trans. A*, 14(1), 211–221, 1983.

858 Barnes, P., Tabor, D. and Walker, J. C. F.: The friction and creep of polycrystalline ice, in *Proceedings of the Royal Society of London A: Mathematical, Physical and Engineering Sciences*, vol. 324, pp. 127–155, The Royal Society, 1971.

861 Barnola, J.-M., Pimienta, P., Raynaud, D. and Korotkevich, Y. S.: CO<sub>2</sub>-climate relationship as deduced  
862 from the Vostok ice core: a re-examination based on new measurements and on a re-evaluation of  
863 the air dating, *Tellus B*, 43(2), 83–90, 1991.

864 Bazin, L., Landais, A., Lemieux-Dudon, B., Toyé Mahamadou Kele, H., Veres, D., Parrenin, F.,  
865 Martinerie, P., Ritz, C., Capron, E., Lipenkov, V., Loutre, M-F., Vinther, B., Svensson, A., Rasmussen,  
866 S. O., Severi, M., Blunier, T., Leuenberger, M., Fischer, H., Masson-Delmotte, V., Chapellaz, J., and  
867 Wolff E.: An optimized multi-proxy, multi-site Antarctic ice and gas orbital chronology (AICC2012):  
868 120-800 ka, *Clim. Past*, 9(4), 1715–1731, 2013.

869 Bender, M. L., Floch, G., Chappellaz, J., Suwa, M., Barnola, J.-M., Blunier, T., Dreyfus, G., Jouzel, J.  
870 and Parrenin, F.: Gas age–ice age differences and the chronology of the Vostok ice core, 0–100 ka,  
871 *J. Geophys. Res.*, 111(D21), doi:10.1029/2005JD006488, 2006.

872 Benson, C. S.: Stratigraphic studies in the snow and firn of the Greenland ice sheet, PhD Thesis,  
873 California Institute of Technology, pp 228, 1960.

874 Bernache-Assollant, D. and Bonnet, J.-P.: Frittage: aspects physico-chimiques - Partie 1: frittage en  
875 phase solide, Ed. Techniques Ingénieur., 2005.



- 876 Blackford, J. R.: Sintering and microstructure of ice: a review, *J. Phys. Appl. Phys.*, 40(21), R355–  
877 R385, doi:10.1088/0022-3727/40/21/R02, 2007.
- 878 Buizert, C., Sowers, T. and Blunier, T.: Assessment of diffusive isotopic fractionation in polar firn, and  
879 application to ice core trace gas records, *Earth Planet. Sci. Lett.*, 361, 110–119,  
880 doi:10.1016/j.epsl.2012.11.039, 2013.
- 881 Buizert, C., Gkinis, V., Severinghaus, J. P., He, F., Lecavalier, B. S., Kindler, P., Leuenberger, M.,  
882 Carlson, A. E., Vinther, B., Masson-Delmotte, V., White, J. W. C., Liu, Z., Otto-Bliesner, B. and Brook,  
883 E. J.: Greenland temperature response to climate forcing during the last deglaciation, *Science*,  
884 345(6201), 1177–1180, doi:10.1126/science.1254961, 2014.
- 885 Buizert, C., Cuffey, K. M., Severinghaus, J. P., Baggenstos, D., Fudge, T. J., Steig, E. J., Markle, B. R.,  
886 Winstrup, M., Rhodes, R. H., Brook, E. J., Sowers, T. A., Clow, G. D., Cheng, H., Edwards, R. L., Sigl,  
887 M., McConnell, J. R. and Taylor, K. C.: The WAIS Divide deep ice core WD2014 chronology-Part 1:  
888 Methane synchronization (68–31 ka BP) and the gas age–ice age difference, *Clim. Past*, 11(2), 153–  
889 173, doi:10.5194/cp-11-153-2015, 2015.
- 890 Capron, E., Landais, A., Buiron, D., Cauquoin, A., Chappellaz, J., Debret, M., Jouzel, J., Leuenberger,  
891 M., Martinerie, P., Masson-Delmotte, V., Mulvaney, R., Parrenin, F. and Prié, F.: Glacial–interglacial  
892 dynamics of Antarctic firn columns: comparison between simulations and ice core air- $\delta^{15}\text{N}$   
893 measurements, *Clim. Past*, 9(3), 983–999, doi:10.5194/cp-9-983-2013, 2013.
- 894 Colbeck, S. C.: Theory of metamorphism of dry snow, *J. Geophys. Res. Oceans*, 88(C9), 5475–5482,  
895 1983.
- 896 Craig, H., Horibe, Y. and Sowers, T.: Gravitational separation of gases and isotopes in polar ice caps,  
897 *Science*, 242(4886), 1675–1678, 1988.
- 898 Cuffey, K. M. and Clow, G. D.: Temperature, accumulation, and ice sheet elevation in central  
899 Greenland through the last deglacial transition, *J. Geophys. Res. Oceans*, 102(C12), 26383–26396,  
900 1997.
- 901 Dahl-Jensen, D.: Past Temperatures Directly from the Greenland Ice Sheet, *Science*, 282(5387), 268–  
902 271, doi:10.1126/science.282.5387.268, 1998.
- 903 Dee, D. P., Uppala, S. M., Simmons, A. J., Berrisford, P., Poli, P., Kobayashi, S., Andrae, U., Balmaseda,  
904 M. A., Balsamo, G., Bauer, P., Bechtold, P., Beljaars, A. C. M., van de Berg, L., Bidlot, J., Bormann, N.,  
905 Delsol, C., Dragani, R., Fuentes, M., Geer, A. J., Haimberger, L., Healy, S. B., Hersbach, H., Hólm, E.  
906 V., Isaksen, I., Kållberg, P., Köhler, M., Matricardi, M., McNally, A. P., Monge-Sanz, B. M., Morcrette,  
907 J.-J., Park, B.-K., Peubey, C., de Rosnay, P., Tavolato, C., Thépaut, J.-N. and Vitart, F.: The ERA-Interim  
908 reanalysis: configuration and performance of the data assimilation system, *Q. J. R. Meteorol. Soc.*,  
909 137(656), 553–597, doi:10.1002/qj.828, 2011.
- 910 Dreyfus, G. B., Jouzel, J., Bender, M. L., Landais, A., Masson-Delmotte, V. and Leuenberger, M.: Firn  
911 processes and  $\delta^{15}\text{N}$ : potential for a gas-phase climate proxy, *Quat. Sci. Rev.*, 29(1–2), 28–42,  
912 doi:10.1016/j.quascirev.2009.10.012, 2010.
- 913 Ebinuma, T. and Maeno, N.: Particle rearrangement and dislocation creep in a snow-densification  
914 process, *J. Phys. Colloq.*, 48(C1), C1-263-C1-269, doi:10.1051/jphyscol:1987137, 1987.



- 915 EPICA community members: Eight glacial cycles from an Antarctic ice core, *Nature*, 429(6992), 623–  
916 628, 2004.
- 917 Freitag, J., Kipfstuhl, S., Laepple, T. and Wilhelms, F.: Impurity-controlled densification: a new model  
918 for stratified polar firn, *J. Glaciol.*, 59(218), 1163–1169, doi:10.3189/2013JoG13J042, 2013.
- 919 Frieler, K., Clark, P. U., He, F., Buizert, C., Reese, R., Ligtenberg, S. R. M., van den Broeke, M. R.,  
920 Winkelmann, R. and Levermann, A.: Consistent evidence of increasing Antarctic accumulation with  
921 warming, *Nat. Clim. Change*, 5(4), 348–352, doi:10.1038/nclimate2574, 2015.
- 922 Fujita, S., Hirabayashi, M., Goto-Azuma, K., Dallmayr, R., Satow, K., Zheng, J. and Dahl-Jensen, D.:  
923 Densification of layered firn of the ice sheet at NEEM, Greenland, *J. Glaciol.*, 60(223), 905–921,  
924 doi:10.3189/2014JoG14J006, 2014.
- 925 Fujita, S., Goto-Azuma, K., Hirabayashi, M., Hori, A., Iizuka, Y., Motizuki, Y., Motoyama, H. and  
926 Takahashi, K.: Densification of layered firn in the ice sheet at Dome Fuji, Antarctica, *J. Glaciol.*,  
927 62(231), 103–123, doi:10.1017/jog.2016.16, 2016.
- 928 Goujon, C., Barnola, J.-M. and Ritz, C.: Modeling the densification of polar firn including heat  
929 diffusion: Application to close-off characteristics and gas isotopic fractionation for Antarctica and  
930 Greenland sites, *J. Geophys. Res. Atmospheres*, 108(D24), 2003.
- 931 Gow, A. J.: Deep core studies of the accumulation and densification of snow at Byrd station and  
932 Little America V, Antarctica, CRREL Research Report 197, 1968.
- 933 Guillevic, M., Bazin, L., Landais, A., Kindler, P., Orsi, A., Masson-Delmotte, V., Blunier, T., Buchardt,  
934 S. L., Capron, E., Leuenberger, M., Martinerie, P., Prié, F. and Vinther, B. M.: Spatial gradients of  
935 temperature, accumulation and  $\delta^{18}\text{O}$ -ice in Greenland over a series of Dansgaard-Oeschger events,  
936 *Clim. Past*, 9(3), 1029–1051, doi:10.5194/cp-9-1029-2013, 2013.
- 937 Hagemuller, P., Chambon, G. and Naaim, M.: Microstructure-based modeling of snow mechanics:  
938 a discrete element approach, *The Cryosphere*, 9(5), 1969–1982, doi:10.5194/tc-9-1969-2015, 2015.
- 939 Helsen, M. M., van den Broeke, M. R., van de Wal, R. S. W., van de Berg, W. J., van Meijgaard, E.,  
940 Davis, C. H., Li, Y. and Goodwin, I.: Elevation Changes in Antarctica Mainly Determined by  
941 Accumulation Variability, *Science*, 320(5883), 1626–1629, doi:10.1126/science.1153894, 2008.
- 942 Herron, M. M. and Langway, C. C.: Firn densification: an empirical model, *J. Glaciol.*, 25(93), 373–  
943 385, 1980.
- 944 Hörhold, M. W., Laepple, T., Freitag, J., Bigler, M., Fischer, H. and Kipfstuhl, S.: On the impact of  
945 impurities on the densification of polar firn, *Earth Planet. Sci. Lett.*, 325, 93–99, 2012.
- 946 Jacka, T. H. and Li, J.: The steady-state crystal size of deforming ice, *Ann. Glaciol.*, 20(1), 13–18, 1994.
- 947 Jouzel, J.: Magnitude of isotope/temperature scaling for interpretation of central Antarctic ice cores,  
948 *J. Geophys. Res.*, 108(D12), doi:10.1029/2002JD002677, 2003.
- 949 Jouzel, J., Masson-Delmotte, V., Cattani, O., Dreyfus, G., Falourd, S., Hoffmann, G., Minster, B.,  
950 Nouet, J., Barnola, J. M., Chappellaz, J., Fischer, H., Gallet, J. C., Johnsen, S., Leuenberger, M.,  
951 Loulergue, L., Luethi, D., Oerter, H., Parrenin, F., Raisbeck, G., Raynaud, D., Schilt, A., Schwander, J.,  
952 Selmo, E., Souchez, R., Spahni, R., Stauffer, B., Steffensen, J. P., Stenni, B., Stocker, T. F., Tison, J. L.,



- 953 Werner, M. and Wolff, E. W.: Orbital and Millennial Antarctic Climate Variability over the Past  
954 800,000 Years, *Science*, 317(5839), 793–796, doi:10.1126/science.1141038, 2007.
- 955 Kapsner, W. R., Alley, R. B., Shuman, C. A., Anandakrishnan, S. and Grootes, P. M.: Dominant  
956 influence of atmospheric circulation on snow accumulation in Greenland over the past 18,000 years,  
957 *Nature*, 373(6509), 52–54, 1995.
- 958 Kindler, P., Guillevic, M., Baumgartner, M., Schwander, J., Landais, A., Leuenberger, M., Spahni, R.,  
959 Capron, E. and Chappellaz, J.: Temperature reconstruction from 10 to 120 kyr b2k from the NGRIP  
960 ice core, *Clim. Past*, 10(2), 887–902, doi:10.5194/cp-10-887-2014, 2014.
- 961 Kojima, K.: Densification of seasonal snow cover, *Phys. Snow Ice Proc. HUSCAP*, 1(2), 929–952, 1967.
- 962 Landais, A., Barnola, J. M., Kawamura, K., Caillon, N., Delmotte, M., Van Ommen, T., Dreyfus, G.,  
963 Jouzel, J., Masson-Delmotte, V., Minster, B., Freitag, J., Leuenberger, M., Schwander, J., Huber, C.,  
964 Etheridge, D. and Morgan, V.: Firn-air  $\delta^{15}\text{N}$  in modern polar sites and glacial–interglacial ice: a  
965 model-data mismatch during glacial periods in Antarctica?, *Quat. Sci. Rev.*, 25(1–2), 49–62,  
966 doi:10.1016/j.quascirev.2005.06.007, 2006.
- 967 Landais, A., Dreyfus, G., Capron, E., Jouzel, J., Masson-Delmotte, V., Roche, D. M., Prié, F., Caillon,  
968 N., Chappellaz, J., Leuenberger, M., Lourantou, A., Parrenin, F., Raynaud, D. and Teste, G.: Two-  
969 phase change in CO<sub>2</sub>, Antarctic temperature and global climate during Termination II, *Nat. Geosci.*,  
970 6(12), 1062–1065, doi:10.1038/ngeo1985, 2013.
- 971 Li, J. and Zwally, H. J.: Modeling the density variation in the shallow firn layer, *Ann. Glaciol.*, 38(1),  
972 309–313, 2004.
- 973 Ligtenberg, S. R. M., Medley, B., Van Den Broeke, M. R. and Munneke, P. K.: Antarctic firn  
974 compaction rates from repeat-track airborne radar data: II. Firn model evaluation, *Ann. Glaciol.*,  
975 56(70), 167–174, doi:10.3189/2015AoG70A204, 2015.
- 976 Lipenkov, V. Y., Barkov, N. I., Duval, P. and Pimienta, P.: Crystalline texture of the 2083 m ice core at  
977 Vostok Station, Antarctica, *J. Glaciol.*, 35(121), 392–398, 1989.
- 978 Louergue, L., Parrenin, F., Blunier, T., Barnola, J.-M., Spahni, R., Schilt, A., Raisbeck, G. and  
979 Chappellaz, J.: New constraints on the gas age–ice age difference along the EPICA ice cores, 0–50 kyr,  
980 *Clim. Past*, 3, 527–540, 2007.
- 981 Louergue, L., Schilt, A., Spahni, R., Masson-Delmotte, V., Blunier, T., Lemieux, B., Barnola, J.-M.,  
982 Raynaud, D., Stocker, T. F. and Chappellaz, J.: Orbital and millennial-scale features of atmospheric  
983 CH<sub>4</sub> over the past 800,000 years, *Nature*, 453(7193), 383–386, doi:10.1038/nature06950, 2008.
- 984 Lüthi, D., Le Floch, M., Bereiter, B., Blunier, T., Barnola, J.-M., Siegenthaler, U., Raynaud, D., Jouzel,  
985 J., Fischer, H., Kawamura, K. and Stocker, T. F.: High-resolution carbon dioxide concentration record  
986 650,000–800,000 years before present, *Nature*, 453(7193), 379–382, doi:10.1038/nature06949,  
987 2008.
- 988 Maeno, N. and Ebinuma, T.: Pressure sintering of ice and its implication to the densification of snow  
989 at polar glaciers and ice sheets, *J. Phys. Chem.*, 87(21), 4103–4110, 1983.
- 990 Marcott, S. A., Bauska, T. K., Buizert, C., Steig, E. J., Rosen, J. L., Cuffey, K. M., Fudge, T. J.,  
991 Severinghaus, J. P., Ahn, J., Kalk, M. L., McConnell, J. R., Sowers, T., Taylor, K. C., White, J. W. C. and



- 992 Brook, E. J.: Centennial-scale changes in the global carbon cycle during the last deglaciation, *Nature*,  
993 514(7524), 616–619, doi:10.1038/nature13799, 2014.
- 994 Martinerie, P., Raynaud, D., Etheridge, D. M., Barnola, J.-M. and Mazaudier, D.: Physical and climatic  
995 parameters which influence the air content in polar ice, *Earth Planet. Sci. Lett.*, 112(1–4), 1–13,  
996 1992.
- 997 Martinerie, P., Lipenkov, V. Y., Raynaud, D., Chappellaz, J., Barkov, N. I. and Lorius, C.: Air content  
998 paleo record in the Vostok ice core (Antarctica): A mixed record of climatic and glaciological  
999 parameters, *J. Geophys. Res. Atmospheres*, 99(D5), 10565–10576, 1994.
- 1000 Mellor, M.: Properties of snow, CRREL Monograph, Section III-A1., 1964.
- 1001 Miller, D. A., Adams, E. E. and Brown, R. L.: A microstructural approach to predict dry snow  
1002 metamorphism in generalized thermal conditions, *Cold Reg. Sci. Technol.*, 37(3), 213–226,  
1003 doi:10.1016/j.coldregions.2003.07.001, 2003.
- 1004 Overly, T. B., Hawley, R. L., Helm, V., Morris, E. M. and Chaudhary, R. N.: Greenland annual  
1005 accumulation along the EGIG line, 1959–2004, from ASIRAS airborne radar and detailed neutron-  
1006 probe density measurements, *Cryosphere Discuss.*, 9(6), 6791–6828, doi:10.5194/tcd-9-6791-2015,  
1007 2015.
- 1008 Parrenin, F., Dreyfus, G., Durand, G., Fujita, S., Gagliardini, O., Gillet, F., Jouzel, J., Kawamura, K.,  
1009 Lhomme, N., Masson-Delmotte, V., Ritz, C., Schwander, J., Shoji, H., Uemura, R., Watanabe, O., and  
1010 Yoshida, N.: 1-D-ice flow modelling at EPICA Dome C and Dome Fuji, East Antarctica, *Clim. Past*, 3(2),  
1011 243–259, 2007.
- 1012 Parrenin, F., Petit, J.-R., Masson-Delmotte, V., Wolff, E., Basile-Doelsch, I., Jouzel, J., Lipenkov, V.,  
1013 Rasmussen, S. O., Schwander, J., Severi, M., Udasti, R., Veres, D. and Vinther, B. M.: Volcanic  
1014 synchronisation between the EPICA Dome C and Vostok ice cores (Antarctica) 0–145 kyr BP, *Clim.*  
1015 *Past*, 8(3), 1031–1045, doi:10.5194/cp-8-1031-2012, 2012.
- 1016 Parrenin, F., Masson-Delmotte, V., Köhler, P., Raynaud, D., Paillard, D., Schwander, J., Barbante, C.,  
1017 Landais, A., Wegner, A., Jouzel, J.: Synchronous change of atmospheric CO<sub>2</sub> and Antarctic  
1018 temperature during the last deglacial warming, *Science*, vol. 339, 1060–1063, 2013.  
1019
- 1020 Pimienta, P.: Etude du comportement mécanique des glaces polycristallines aux faibles contraintes:  
1021 applications aux glaces des calottes polaires, PhD Thesis, Université Scientifique Technologique et  
1022 Médicale de Grenoble., 166 pp, 1987.
- 1023 Pimienta, P. and Duval, P.: Rate controlling processes in the creep of the polar glacier ice, *J. Phys.*  
1024 *Colloq.*, 48(C1), C1-243–C1-248, doi:10.1051/jphyscol:1987134, 1987.
- 1025 Proksch, M., Rutter, N., Fierz, C. and Schneebeli, M.: Intercomparison of snow density  
1026 measurements: bias, precision, and vertical resolution, *The Cryosphere*, 10(1), 371–384,  
1027 doi:10.5194/tc-10-371-2016, 2016.
- 1028 Ramseier, R. O.: Self-diffusion in ice monocrystals, CRREL Research Report no 232, 1967.
- 1029 Rasmussen, S. O., Andersen, K. K., Svensson, A. M., Steffensen, J. P., Vinther, B. M., Clausen, H. B.,  
1030 Siggaard-Andersen, M.-L., Johnsen, S. J., Larsen, L. B., Dahl-Jensen, D., Bigler, M., Röthlisberger, R.,



- 1031 Fischer, H., Goto-Azuma, K., Hansson, M. E. and Ruth, U.: A new Greenland ice core chronology for  
1032 the last glacial termination, *J. Geophys. Res.*, 111(D6), doi:10.1029/2005JD006079, 2006.
- 1033 Rhodes, R. H., Brook, E. J., Chiang, J. C., Blunier, T., Maselli, O. J., McConnell, J. R., Romanini, D. and  
1034 Severinghaus, J. P.: Enhanced tropical methane production in response to iceberg discharge in the  
1035 North Atlantic, *Science*, 348(6238), 1016–1019, 2015.
- 1036 Salamatin, A. N., Lipenkov, V. Y., Barnola, J. M., Hori, A., Duval, P. and Hondoh, T.: Snow/firn  
1037 densification in polar ice sheets, *Phys. Ice Core Rec. - II*, 68(Supplement), 195–222, 2009.
- 1038 Schwander, J.: The transformation of snow to ice and the occlusion of gases, *Environ. Rec. Glaciers*  
1039 *Ice Sheets*, 53–67, 1989.
- 1040 Schwander, J., Sowers, T., Barnola, J.-M., Blunier, T., Fuchs, A. and Malaizé, B.: Age scale of the air  
1041 in the summit ice: Implication for glacial-interglacial temperature change, *J. Geophys. Res.*  
1042 *Atmospheres*, 102(D16), 19483–19493, 1997.
- 1043 Severinghaus, J. P., Sowers, T., Brook, E. J., Alley, R. B. and Bender, M. L.: Timing of abrupt climate  
1044 change at the end of the Younger Dryas interval from thermally fractionated gases in polar ice,  
1045 *Nature*, 391(6663), 141–146, 1998.
- 1046 Sowers, T., Bender, M. and Raynaud, D.: Elemental and isotopic composition of occluded O<sub>2</sub> and N<sub>2</sub>  
1047 in polar ice, *J. Geophys. Res. Atmospheres*, 94(D4), 5137–5150, 1989.
- 1048 Sowers, T., Bender, M. and Korotkevich, Y.:  $\delta^{15}\text{N}$  of N<sub>2</sub> in Air Trapped in Polar ice, *J. Geophys. Res.*,  
1049 97(D14), 15–683, 1992.
- 1050 Veres, D., Bazin, L., Landais, A., Toyé Mahamadou Kele, H., Lemieux-Dudon, B., Parrenin, F.,  
1051 Martinerie, P., Blayo, E., Blunier, T., Capron, E., Chappellaz, J., Rasmussen, S. O., Seeri, M., Svensson,  
1052 A., Vinther, B., and Wolff, E. W.: The Antarctic ice core chronology (AICC2012): an optimized multi-  
1053 parameter and multi-site dating approach for the last 120 thousand years, *Clim. Past*, 9(4), 1733–  
1054 1748, 2013.
- 1055 WAIS Divide Project Members: Onset of deglacial warming in West Antarctica driven by local orbital  
1056 forcing, *Nature*, 500(7463), 440–444, doi:10.1038/nature12376, 2013.
- 1057 WAIS Divide Project Members: Precise inter-polar phasing of abrupt climate change during the last  
1058 ice age, *Nature*, 520(7549), 661–665, 2015.
- 1059 Wilkinson, D. S. and Ashby, M. F.: Pressure sintering by power law creep, *Acta Metall.*, 23(11), 1277–  
1060 1285, 1975.
- 1061 Witrant, E., Martinerie, P., Hogan, C., Laube, J. C., Kawamura, K., Capron, E., Montzka, S. A.,  
1062 Dlugokencky, E. J., Etheridge, D., Blunier, T. and Sturges, W. T.: A new multi-gas constrained model  
1063 of trace gas non-homogeneous transport in firn: evaluation and behaviour at eleven polar sites,  
1064 *Atmospheric Chem. Phys.*, 12(23), 11465–11483, doi:10.5194/acp-12-11465-2012, 2012.
- 1065 Zwally, H. J. and Li, J.: Seasonal and interannual variations of firn densification and ice-sheet surface  
1066 elevation at the Greenland summit, *J. Glaciol.*, 48(161), 199–207, 2002.